







**Please cite the Published Version**

Becerra, R , Azurdia-Meza, CA , Palacios Játiva, P , Soto, I , Sandoval, J , Ijaz, M   
and Carrera, DF (2023) A Wavelength-Dependent Visible Light Communication Channel Model for Underground Environments and Its Performance Using a Color-Shift Keying Modulation Scheme. Electronics, 12 (3). 577 ISSN 2079-9292

**DOI:** <https://doi.org/10.3390/electronics12030577>

**Publisher:** MDPI AG

**Version:** Published Version

**Downloaded from:** <https://e-space.mmu.ac.uk/636284/>

**Usage rights:**  [Creative Commons: Attribution 4.0](https://creativecommons.org/licenses/by/4.0/)

**Additional Information:** This is an open access article which first appeared in Electronics, published by MDPI

**Data Access Statement:** The data presented in this study are available on request from the corresponding author.

**Enquiries:**

If you have questions about this document, contact [openresearch@mmu.ac.uk](mailto:openresearch@mmu.ac.uk). Please include the URL of the record in e-space. If you believe that your, or a third party's rights have been compromised through this document please see our Take Down policy (available from <https://www.mmu.ac.uk/library/using-the-library/policies-and-guidelines>)

## Article

# A Wavelength-Dependent Visible Light Communication Channel Model for Underground Environments and Its Performance Using a Color-Shift Keying Modulation Scheme

Raimundo Becerra <sup>1</sup>, Cesar A. Azurdia-Meza <sup>1,\*</sup>, Pablo Palacios Játiva <sup>1,2</sup>, Ismael Soto <sup>3</sup>, Jorge Sandoval <sup>1</sup>, Muhammad Ijaz <sup>4</sup> and Diego Fernando Carrera <sup>5</sup>

<sup>1</sup> Department of Electrical Engineering, Universidad de Chile, Santiago 8370451, Chile

<sup>2</sup> Escuela de Informática y Telecomunicaciones, Universidad Diego Portales, Santiago 8370190, Chile

<sup>3</sup> Department of Electrical Engineering, Universidad de Santiago de Chile, Santiago 9170124, Chile

<sup>4</sup> School of Engineering, Manchester Metropolitan University, Manchester M15 6BH, UK

<sup>5</sup> School of Technologies, Universidad Tecnológica Empresarial de Guayaquil, Guayaquil 090511, Ecuador

\* Correspondence: cazurdia@ing.uchile.cl; Tel.: +56-2-2978-4193

**Abstract:** Reliable wireless communications are crucial for ensuring workers' safety in underground tunnels and mines. Visible light communications (VLC) have been proposed as auxiliary systems for short-range wireless communications in underground environments due to their seamless availability, immunity to electromagnetic interference, and illumination capabilities. Although multiple VLC channel models have been proposed for underground mines (UM) so far, none of these models have considered the wavelength dependence of the underground mining VLC channel (UM-VLC). In this paper, we propose a single-input, single-output (SISO), wavelength-dependent UM-VLC channel model considering the wavelength dependence of the light source, reflections, light scattering, and the attenuation due to dust and the photodetector. Since wavelength dependence allows us to model VLC systems more accurately with color-based modulation, such as color-shift keying (CSK), we also propose a wavelength-dependent CSK-based UM-VLC channel model. We define a simulation scenario in an underground mine roadway and calculate the received power, channel impulse response (CIR), signal-to-noise ratio (SNR), signal-to-interference ratio (SIR), root mean square (RMS) delay, and bit error rate (BER). For comparison, we also calculate these parameters for a monochromatic state-of-the-art UM-VLC channel and use it as a reference channel. We find that the inclusion of wavelength-dependency in CSK-based UM-VLC systems plays a significant role in their performance, introducing color distortion that the color calibration algorithm defined in the IEEE 802.15.7 VLC standard finds harder to revert than the linear color distortion induced by monochromatic CSK channels.

**Keywords:** color-shift keying modulation; Mie scattering and absorption; underground mining visible light communication (UM-VLC); visible light communication (VLC) channel modeling; wavelength-dependent communication systems



**Citation:** Becerra, R.; Azurdia-Meza, C.A.; Palacios Játiva, P.; Soto, I.; Sandoval, J.; Ijaz, M.; Carrera, D.F. A Wavelength-Dependent Visible Light Communication Channel Model for Underground Environments and Its Performance Using a Color-Shift Keying Modulation Scheme.

*Electronics* **2023**, *12*, 577. <https://doi.org/10.3390/electronics12030577>

Academic Editor: Shlomi Arnon

Received: 8 December 2022

Revised: 13 January 2023

Accepted: 19 January 2023

Published: 23 January 2023



**Copyright:** © 2023 by the authors. Licensee MDPI, Basel, Switzerland. This article is an open access article distributed under the terms and conditions of the Creative Commons Attribution (CC BY) license (<https://creativecommons.org/licenses/by/4.0/>).

## 1. Introduction

Underground mining (UM) is considered a sector in which worker health is at high risk [1]. In an underground mine, miners are constantly exposed to a harsh work environment with unique characteristics such as high humidity, temperature, hazardous gas and dust concentrations, and noise, as well as poor visibility [2]. These factors negatively impact miners' mental and physical health in the long term, in addition to the fact that the work scenario is subject to unpredictable hazards such as fires, explosions, roof collapses, earthquakes, toxic gas leaks, floods, and vehicle accidents that could cause serious injuries or disabilities, and in the worst cases, fatalities [3]. Reliable wireless communication systems play a significant role in maintaining miners' safety. Applications such as mobile

two-way voice communications and tracking miners' locations are crucial in an emergency, while monitoring systems for air quantity and hazardous gas and dust concentration ensure worker safety throughout the mine operation [4].

As the most widely used type of wireless communication, radio frequency (RF) communications suffer from severe electromagnetic interference (EMI): equipment used during normal mining operations such as drill machines, mine trucks, electric motors, and continuous miners operate in the same frequency range as radio communication devices, causing a significant amount of noise [4]. To complement the classical wireless communication systems deployed in UM, researchers have proposed the use of visible light communications (VLC), in which a light-emitting diode (LED) is intensity-modulated by a driving current at the transmitter (TX), producing a visible light signal that is detected by a photodiode (PD) that produces a photocurrent at the receiver (RX). The optical signal is modulated rapidly enough to be not perceived by the human eye, making VLC systems suitable for data transmission and illumination at the same time. Its immunity to EMI, relatively low cost, unlicensed frequency spectrum, support of high data rates, and the fact that underground mines already depend on artificial light sources for their functioning make VLC an attractive candidate for short-range wireless communications in underground mines [5,6].

Although the VLC channel for classical indoor environments (i.e., regular buildings) has been studied well, the underground mining VLC channel (UM-VLC) has only recently been a topic of research interest. Over the past few years, several authors have proposed UM-VLC channel models that account for channel characteristics inherent to the UM environment that are not present in classical indoor environments. These include, but are not limited, to the relative tilt and rotation between LED and PD, irregular (i.e., non-flat) walls, light scattering and absorption due to dust, and shadowing (e.g., large machinery blocking the light signal) [7,8]. However, to the best of the authors' knowledge, no UM-VLC channel model has been proposed in the literature that accounts for the wavelength's dependence of the aforementioned phenomena or the inherent spectral properties of LEDs and PDs. Although VLC channel models that do not account for wavelength dependency are suitable for VLC systems with monochromatic or narrowband light sources, illumination systems require white-light LEDs that are inherently wideband. Miramirkhani and Uysal [9] argue that the wideband property of white light LEDs calls for the inclusion of wavelength dependency in VLC channel modeling and proceed to mention multiple research papers that propose wavelength-dependent classical in-door VLC channels.

Furthermore, wavelength dependency becomes an even more important factor when considering color-domain-based VLC systems, in which the wavelength dependence of the channel is crucial to the system's performance. The most notable color-domain-based modulation scheme is known as color shift keying (CSK) modulation, in which data are encoded into the instantaneous optical power of RGB LEDs in such a way that the perceived color and the average transmitted optical are static [10]. This modulation scheme is included in the IEEE 802.15.7 standard [11] for high-data-rate applications with multiple light sources, where 4-CSK, 8-CSK, and 16-CSK constellations are defined. Most of the existing literature on the performance and channel modeling of CSK-based VLC systems considers classical indoor VLC channels with only a line-of-sight (LOS) component. Notable exceptions include the outdoor optical camera communications channel (OOC) [12], the underwater optical communication channel (UWOOC) [13], and the underwater wireless optical communication channel (UWOC) [14]. To the best knowledge of the authors, CSK-based UM-VLC systems have not been modeled or evaluated in the literature so far.

In this work, we propose a wavelength-dependent UM-VLC single-input, single-output (SISO) channel model in which the spectral characteristics of the LED, the PD, the dust particles, and the reflective surfaces are considered. The UM-VLC channel model based on ray tracing proposed by Palacios et al. [7] is used as a starting point, from which the LED/PD tilt and rotation model, the shadowing model, and the irregular wall model are inherited. Additionally, we include a dust scattering and absorption model based on Mie theory, which has already been considered in state-of-the-art UM-VLC channel

models such as the one presented by Javaid et al. [5], although without considering its spectral characteristics.

The proposed wavelength-dependent UM-VLC channel model allows us to define a CSK-based UM-VLC channel model very naturally. A simulation scenario with appropriate parameters is implemented to evaluate the CSK-based UM-VLC system in terms of the average received optical power, the signal-to-interference ratio (SIR), the signal-to-noise ratio (SNR), the channel impulse response (CIR), the root mean square (RMS) delay, and the bit error rate (BER). With these metrics, the performance of the CSK-based UM-VLC system was compared with the performance achieved under the reference channel proposed by [7].

The contributions of this paper can be summarized as follows:

- A novel wavelength-dependent SISO UM-VLC channel model is proposed, taking into account LED/PD relative tilt and rotation, irregular walls, shadowing, light scattering, absorption, and their respective spectral characteristics. The LED is modeled as a Lambertian light source and the ray tracing method is used.
- A novel wavelength-dependent CSK-based UM-VLC channel model is proposed on the basis of the proposed wavelength-dependent SISO UM-VLC channel model.
- The performance of the proposed CSK-based UM-VLC channel model is evaluated in a simulated environment, obtaining parameters such as the average received optical power, SIR, SNR, CIR, RMS delay, and BER. The proposed model is then compared to a reference state-of-the-art UM-VLC channel model.

The paper is structured as follows: Section 1 presents a brief introduction and gives a review of the various UM-VLC channel models presented in the literature. Section 2 defines important concepts in the topics of VLC and CSK necessary for contextualizing the rest of the text, while also defining the UM-VLC channel model proposed in this paper. Section 3 presents the simulation results and discusses them. Finally, the conclusions are provided in Section 4.

#### *Related Work*

Due to the relative hostility of mines compared to classical indoor environments, various channel models have been proposed for UM-VLC systems. In Ref. [15], the authors propose a geometric-based deterministic model (GBDM) considering the LOS and NLOS components for a coal mine's workface with hydraulic support metal columns along its footpath. The authors considered the reflections of the metal columns, roof, and floor. Additionally, they also derive the optimal TX location that maximizes the coupled energy of the light signals blocked by the metal columns. The authors also studied the degrading effect of coal dust on the optical signal, employing Mie theory for modeling light scattering and absorption.

The authors of [16] have proposed a recursive UM-VLC channel model that considers light scattering and absorption due to particles and shadowing caused by people. They simulate both a mining roadway and a workface scenario containing multiple transmitters modeled as ideal Lambertian sources and obtain the path loss and RMS delay for the LOS and NLOS links, considering multiple link ranges. Mie theory is used to model light attenuation caused by dust, and a bimodal Gaussian distribution (BGD) is used to model shadowing phenomena.

In Ref. [17], the authors present a VLC channel model for underground tunnels in general. They focus their attention on the relative orientation of LEDs and PDs and their effect on the irradiance and incidence angles, proposing a Lambertian VLC channel model that considers an LOS component dependent on the azimuthal (tilt) and polar (rotation) angles of LEDs and PDs and a diffuse NLOS component independent of the PD's incident angle. They provide simulation results in a tunnel scenario in terms of the symbol error rate (SER) for a VLC link based on pulse amplitude modulation (PAM).

In Refs. [7,18,19], the authors propose a ray-tracing-based UM-VLC channel considering a Lambertian light source, arbitrary LED and PD tilt and rotation angles, reflections on non-flat irregular walls, scattering due to dust particles, and shadowing due to large

machinery. The LED/PD tilt and rotation modeling is taken from [17]. The irregularity of the walls is modeled by discretizing the walls into a grid with small wall segments, each with nondeterministic azimuthal and polar angles. The shadowing effect is modeled as a weighting parameter in the LOS and NLOS links and is calculated as the expected value of a Poisson process which describes the random entry of light-blocking objects into the simulation scenario. The light scattering is modeled as a combination of Rayleigh and Mie regimes, with dust particles randomly distributed around the PD in a two-dimensional disk in [7] and in a hemispheric three-dimensional region in [18]. The light-degrading effects of scattering are not factored into the LOS and reflection-induced NLOS links; instead, another NLOS channel link is modeled, induced by the scattered light, in what could be called a scattering-induced NLOS link. Scattering-induced NLOS links are common in optical communication channels where TX and RX are blocked by obstacles or the LOS link cannot be guaranteed [20], whereas it is not common in VLC channels since the LOS link is usually available. In Ref. [7], the proposed channel model was evaluated in a simulated UM tunnel. The resulting CIR, received optical power, and RMS delay were presented and compared with a referential classical indoor VLC channel model. In Ref. [18], the same simulated environment was used, with CIR, received optical power, SNR, RMS delay, and BER being presented for different amounts of modeled dust particles, and compared to the proposed channel model in [7], considering on-off keying (OOK) modulation.

In Ref. [5], the authors propose a UM-VLC channel based on ray tracing for coal mines, considering a Lambertian light source, scattering, and absorption of light and shadowing. Mie theory is used to model the scattering and absorption due to coal dust, while shadowing is modeled using a BGD. Simulations are performed in a mine gallery and sub-gallery where the resulting path loss, received power, RMS delay, SNR, and probability of error are presented and analyzed as a function of link distance. The CIR is also presented for the two simulation scenarios.

In Table 1, the aforementioned UM-VLC channel models are compared in terms of how many UM-related factors they consider. It is clear that there is a gap in the study of wavelength dependence in the context of UM-VLC channels that this present paper seeks to remediate. Wavelength-dependent channels have been proposed in all kinds of optical communication systems. For instance, wavelength-dependent optical channels have been proposed for classical indoor VLCs in empty rooms [21] and in rooms with objects [22] and for UWOC [23], to name a few.

**Table 1.** Comparison of the proposed model with other state-of-the-art UM-VLC channel models.

Model	Characteristics					
	LED/PD Tilt/Rotation	Irregular Walls	Shadowing	Scattering by Dust	Absorption by Dust	Wavelength Dependence
Palacios et al., 2022 [18]	✓	✓	✓	✓	✗	✗
Javaid et al., 2021 [5]	✗	✗	✓	✓	✓	✗
Palacios et al., 2020 [7]	✓	✓	✓	✓	✗	✗
Morales and García, 2019 [17]	✓	✗	✗	✗	✗	✗
Wang et al., 2018 [16]	✗	✗	✓	✓	✓	✗
Zhai and Zhang, 2015 [15]	✗	✗	✓	✓	✓	✗
Our proposal	✓	✓	✓	✓	✓	✓

## 2. Materials and Methods

### 2.1. General VLC Link

Given a monochromatic LED producing an optical power signal  $x(t)$ , the photocurrent  $y(t)$  detected at the PD is given by

$$y(t) = Rh(t) * x(t) + n(t), \quad (1)$$

where  $*$  is the convolution operation,  $R$  is the PD responsivity, and  $n(t)$  is the additive noise. In this work, we will refer to  $h(t)$  as the optical channel (optical input, optical output), and  $Rh(t)$  as the electro-optical channel (optical input, electrical output). Since  $x(t)$  represents the optical power, we find that it must be non-negative, i.e.,

$$x(t) \geq 0, \quad \forall t. \quad (2)$$

Furthermore, the illumination requirement implies that the average transmitted optical power must remain at a constant optical power  $P_{\text{avg}}$ , given by [24]

$$P_{\text{avg}} = \lim_{T \rightarrow \infty} \frac{1}{2T} \int_{-T}^T x(t) dt. \quad (3)$$

The optical signal is also bounded by the optical power produced by the LED at the peak drive current,  $P_{\text{peak}}$ , i.e.,

$$x(t) \leq P_{\text{peak}}, \quad \forall t. \quad (4)$$

An important element of the VLC channel model is the optical DC gain,  $H(0)$ , given by

$$H(0) = \int_0^{\infty} h(t) dt. \quad (5)$$

Equivalently, the electro-optical DC gain is given by  $RH(0)$ . Modeling the channel DC gain is desired because it allows us to obtain the received optical power  $P_R$  and produced photocurrent  $I_{\text{ph}}$  at the PD for a given transmitted optical power  $P_T$  by [25]

$$P_R = H(0)P_T \quad \text{and} \quad I_{\text{ph}} = RH(0)P_T. \quad (6)$$

### 2.2. CSK Modulation

Color-shift keying is a VLC modulation scheme involving multiple LEDs, in which the average emitted optical color and the total optical power are kept constant. It is included in the IEEE 802.15.7 standard for short-range optical wireless communications as part of the PHY III mode of the VLC physical layer, which is used for high-data-rate applications in indoor environments [11].

A CSK-based system consists of three RGB LEDs, each transmitting a primary color, red, green, or blue, and three PDs with optical filters that let through one of the primary colors each. CSK symbols are defined in the CIE 1931  $xy$  color space. The center-of-band wavelengths of the three LEDs  $\lambda_r, \lambda_g, \lambda_b$  are expressed in CIE 1931  $xy$  space coordinates by

$$\mathbf{s}_r = \begin{bmatrix} x_r \\ y_r \end{bmatrix}, \quad \mathbf{s}_g = \begin{bmatrix} x_g \\ y_g \end{bmatrix}, \quad \mathbf{s}_b = \begin{bmatrix} x_b \\ y_b \end{bmatrix}, \quad (7)$$

respectively.  $\mathbf{s}_r, \mathbf{s}_g$ , and  $\mathbf{s}_b$  are known as the center-of-band symbols. All colors that can be reproduced by the three LEDs via additive mixing form a triangle in the CIE  $xy$  space, with  $\mathbf{s}_r, \mathbf{s}_g$ , and  $\mathbf{s}_b$  being the vertices. The set of all the colors reproducible by the three LEDs is known as the gamut of the system and can be expressed mathematically as the convex combination of the center of band symbols in the CIE  $xy$  space, as in

$$G = \{\alpha_1 \mathbf{s}_r + \alpha_2 \mathbf{s}_g + \alpha_3 \mathbf{s}_b \in \mathbb{R}^2 \mid \alpha_1 + \alpha_2 + \alpha_3 = 1, \quad \alpha_1, \alpha_2, \alpha_3 \geq 0\}, \quad (8)$$

where  $G$  is the gamut of the system. The CSK scheme encodes  $k$  bits per symbol, employing a constellation  $\mathcal{A}$  of  $M = 2^k$  symbols, with  $\mathcal{A} = \{\mathbf{s}_1, \dots, \mathbf{s}_M\}$ , which is known as  $M$ -CSK modulation. Each  $n$ th symbol for  $n = 1 \dots, M$  is a CIE 1931  $xy$  space coordinate inside gamut  $G$ , i.e.,

$$\mathbf{s}_n = \begin{bmatrix} x_n \\ y_n \end{bmatrix} \in G, \quad \forall n = 1, \dots, M. \tag{9}$$

In theory, an infinite number of gamuts and constellations can be defined in the system. However, the IEEE 802.15.7 standard considers only fourteen possible system gamuts and establishes a set of rules to construct symbol constellations given the number of symbols  $M$  and the system gamut  $G$ . The ruleset for constellation construction is laid out in [11]. All possible gamuts and system constellations for 4-CSK, 8-CSK, and 16-CSK, together with their corresponding data mapping, as defined by the IEEE 802.15.7 standard, are presented in [26].

Consider a CSK RGB luminary whose average transmitted optical power must not exceed  $P_{\text{avg}}$ . In order to transmit symbol  $\mathbf{s}_n = [x_n, y_n]^T \in G$ , it must be converted into an optical power triplet  $[P_{1,n}, P_{2,n}, P_{3,n}]^T$  such that

$$P_{1,n} + P_{2,n} + P_{3,n} = P_{\text{avg}} \tag{10}$$

where  $P_{1,n}$ ,  $P_{2,n}$ , and  $P_{3,n}$  are the transmitted optical powers of the red, green, and blue LEDs, respectively, when symbol  $\mathbf{s}_n$  is transmitted. As in [11], the triplet can be found by solving the following system of equations:

$$\begin{aligned} x_n &= \bar{P}_1 x_r + \bar{P}_2 x_g + \bar{P}_3 x_b \\ y_n &= \bar{P}_1 y_r + \bar{P}_2 y_g + \bar{P}_3 y_b \\ 1 &= \bar{P}_1 + \bar{P}_2 + \bar{P}_3. \end{aligned} \tag{11}$$

Consider  $\bar{P}_{1,n}$ ,  $\bar{P}_{2,n}$ , and  $\bar{P}_{3,n}$  to be the solution to Equation (11). Then, the desired optical power triplet for symbol  $\mathbf{s}_n$  is given by

$$\begin{bmatrix} P_{1,n} \\ P_{2,n} \\ P_{3,n} \end{bmatrix} = P_{\text{avg}} \begin{bmatrix} \bar{P}_{1,n} \\ \bar{P}_{2,n} \\ \bar{P}_{3,n} \end{bmatrix}. \tag{12}$$

This also implies that the possible optical power values emitted by the LEDs are bounded by  $P_{\text{avg}}$ , i.e.,

$$0 \leq P_{1,n} \leq P_{\text{avg}}, \quad 0 \leq P_{2,n} \leq P_{\text{avg}}, \quad 0 \leq P_{3,n} \leq P_{\text{avg}}, \quad \forall n = 1, \dots, M. \tag{13}$$

Additionally, in all CSK constellations allowed by the IEEE 802.15.7 standard, the optical power transmitted by each LED averaged over all possible symbols is given by [27]

$$\frac{1}{M} \sum_{n=1}^M P_{1,n} = \frac{1}{M} \sum_{n=1}^M P_{2,n} = \frac{1}{M} \sum_{n=1}^M P_{3,n} = \frac{P_{\text{avg}}}{3}. \tag{14}$$

Given a CSK optical power signal  $\mathbf{x}(t) = [x_1(t), x_2(t), x_3(t)]^T$  (W) as input, where  $x_1(t)$ ,  $x_2(t)$ ,  $x_3(t)$  represent the instantaneous emitted power from the red, green, and blue LED, respectively, we can calculate the instantaneous photocurrent signal  $\mathbf{y}(t) = [y_1(t), y_2(t), y_3(t)]^T$  (A), where  $y_1(t)$ ,  $y_2(t)$ , and  $y_3(t)$  represent the instantaneous photocurrent produced at the red, green, and blue PD, respectively, by

$$y_j(t) = \sum_{i=1}^3 h[i, j](t) * x_i(t) + n_j(t), \quad i, j = 1, 2, 3, \tag{15}$$

where  $n_j(t)$  is the additive noise at the  $j$ th PD with noise variance  $\sigma_j^2$ . The average optical power emitted by the  $i$ th LED,  $P_{\text{avg}, i}$ , is given by

$$P_{\text{avg}, i} = \lim_{T \rightarrow \infty} \frac{1}{2T} \int_{-T}^T x_i(t) dt. \quad (16)$$

From Equation (14), it follows that

$$P_{\text{avg}, 1} = P_{\text{avg}, 2} = P_{\text{avg}, 3} = \frac{P_{\text{avg}}}{3}, \quad (17)$$

where  $P_{\text{avg}}$  is the total average optical power emitted by the TX and is given by

$$P_{\text{avg}} = \lim_{T \rightarrow \infty} \frac{1}{2T} \int_{-T}^T \sum_{i=1}^3 x_i(t) dt. \quad (18)$$

In high-speed VLC schemes, such as CSK-based VLC systems, the impulse response of the LED must be considered [25]. By denoting the impulse response of the LEDs as  $h_{\text{LED}}(t)$ , Equation (15) can be rewritten as

$$y_j(t) = \sum_{i=1}^3 h_{\text{LED}}(t) * h[i, j](t) * x_i(t) + n_j(t), \quad (19)$$

where  $\max_t(h_{\text{LED}}(t)) = 1$ . The DC gain of the electro-optical channel, between the  $i$ th LED and  $j$ th PD,  $H_0^{\text{el}}[i, j]$ , is given by

$$H_0^{\text{el}}[i, j] = \int_0^{\infty} h[i, j](t) dt. \quad (20)$$

In this context, we can define the average photocurrent produced at the  $j$ th PD due to light coming from the  $i$ th LED,  $I_{\text{avg}}[i, j]$ , as

$$I_{\text{avg}}[i, j] = H_0^{\text{el}}[i, j] \cdot P_{\text{avg}, i}. \quad (21)$$

In the VLC literature, additive noise is usually decomposed into the two dominant sources of noise in the VLC link: thermal noise and shot noise. The former, also known as Johnson–Nyquist noise, accounts for the thermal fluctuation (i.e., the temperature) in the particles that constitute the receiver electronics. The later accounts for the noise caused by the fluctuation in the number of photons that hit the  $j$ th PD within a certain time unit. Thermal noise is modeled as additive white Gaussian noise (AWGN), since it is the result of many independent events (thermal fluctuation of individual electrons). Similarly, shot noise is well approximated by AWGN thanks to the central limit theorem, as it is the superposition of a large number of independent events (photons hitting the PD at different times) [28]. With this in mind, and considering that thermal noise and shot noise are statistically independent, the noise variance can be further decomposed as follows:

$$\sigma_j^2 = \sigma_{\text{shot}, j}^2 + \sigma_{\text{thermal}}^2, \quad (22)$$

where  $\sigma_{\text{shot}, j}^2$  is the shot noise variance, and  $\sigma_{\text{thermal}}^2$  is the thermal noise variance. If we assume that there is an electrical filter that follows the PD and that the receiver circuit is a p-i-n/FET transimpedance receiver, then the shot noise variance can be expressed as [29]

$$\sigma_{\text{shot}, j}^2 = 2qB \sum_{i=1}^3 I_{\text{avg}}[i, j] + 2qI_{\text{bg}}I_2B, \quad (23)$$



where  $q$  is the electronic charge constant,  $B$  is the bandwidth of the electrical filter following the PD,  $I_{bg}$  is the photocurrent due to background radiation, and  $I_2 = 0.562$  is known as the noise bandwidth factor. The thermal noise variance can be expressed as [29]

$$\sigma_{\text{thermal}}^2 = \frac{8\pi\kappa T_k}{G_{ol}} C_{pd} A_R I_2 B^2 + \frac{16\pi^2 \kappa T_k \Gamma}{g_m} C_{pd}^2 A_R^2 I_3 B^3, \quad (24)$$

where  $\kappa$  is the Boltzmann constant,  $T_k$  is the absolute temperature,  $G_{ol}$  is the gain in open-loop voltage,  $C_{pd}$  is the fixed capacitance of PD per unit area,  $\Gamma$  is the noise factor of the FET channel,  $g_m$  is the transconductance of the FET, and  $I_3 = 0.0868$  is another factor of noise bandwidth.

Assuming that the additive noise is AWGN, then the electrical SNR for the  $j$ th PD,  $\text{SNR}_{\text{el},j}$ , is given by [24]

$$\text{SNR}_{\text{el},j} = \frac{(I_{\text{avg}}[j,j])^2}{\sigma_j^2}. \quad (25)$$

The electrical signal-to-interference ratio (SIR) for the  $j$ th PD,  $\text{SIR}_{\text{el},j}$ , is given by

$$\text{SIR}_{\text{el},j} = \frac{(I_{\text{avg}}[j,j])^2}{\sum_{i \neq j} (I_{\text{avg}}[i,j])^2}, \quad (26)$$

where the photocurrent induced in the  $j$ th PD by the two other color channels can be modeled as co-channel interference.

### 2.3. Reference UM-VLC Channel Model

The UM-VLC SISO channel model proposed in [7] is used as the reference channel. This channel model considers a monochromatic LED as a generalized Lambertian light source, a PD pair rotated and tilted to each other, irregular walls (i.e., non-flat), shadowing, and a scattering component. Taking into account an optical input and an optical output, the DC gain of the channel model is given by

$$H_{\text{ref,opt}} = H_{\text{LOS}} + H_{\text{NLOS,(1)}} + H_{\text{scatter}}, \quad (27)$$

where  $H_{\text{LOS}}$  represents the LOS component,  $H_{\text{NLOS,(1)}}$  represents the single-hop NLOS component, and  $H_{\text{scatter}}$  represents the contribution of NLOS of light scattering off dust particles. Only one hop is considered, since subsequent bounces are almost negligible in terms of received power and time dispersion [7]. The DC gain of the electro-optical channel model, i.e., when taking into account an optical input and an electrical output, is given by

$$H_{\text{ref,el}} = R(H_{\text{LOS}} + H_{\text{NLOS,(1)}} + H_{\text{scatter}}). \quad (28)$$

Figure 1 presents an illustration of the reference channel model and serves as a companion to the following sections.

#### 2.3.1. Geometry

Before defining the channel components, it is convenient to define some geometrical parameters. Let us consider an underground tunnel of dimensions  $L_x \times L_y \times L_z$  (m), corresponding to its length ( $x$ -axis), width ( $y$ -axis), and height ( $z$ -axis), respectively. The TX or LED is positioned in the fixed coordinates  $\mathbf{T} = [x_{\text{tx}}, y_{\text{tx}}, z_{\text{tx}}]^T$  (m), whereas the receiver position (RX) or the PD position,  $\mathbf{R} = [x_{\text{rx}}, y_{\text{rx}}, z_{\text{rx}}]^T$  (m), can vary. Having defined these parameters, the distance between the LOS links,  $d$ , is given by

$$d = \|\mathbf{R} - \mathbf{T}\|. \quad (29)$$

Consider  $\mathbf{n}_{\text{tx}} = [n_{\text{tx}}^x, n_{\text{tx}}^y, n_{\text{tx}}^z]^T$  as the TX normal vector and  $\mathbf{n}_{\text{rx}} = [n_{\text{rx}}^x, n_{\text{rx}}^y, n_{\text{rx}}^z]^T$  as the RX normal vector. Using the same definitions as [7], the RX tilt angle,  $\beta_{\text{rx}}$ , is defined as

the angle from the z-axis vector,  $[0, 0, 1]^T$  to  $\mathbf{n}_{rx}$ , whereas the TX tilt angle,  $\beta_{tx}$ , is defined as the angle from the negative z-axis vector,  $[0, 0, -1]^T$  to  $\mathbf{n}_{tx}$ . Both tilt angles' definitions are illustrated in Figure 1b. Assuming that TX is higher on the z-axis than RX, then we want the tilt angles to have values  $\beta_{tx}, \beta_{rx} \in [0, \frac{\pi}{2}]$ .

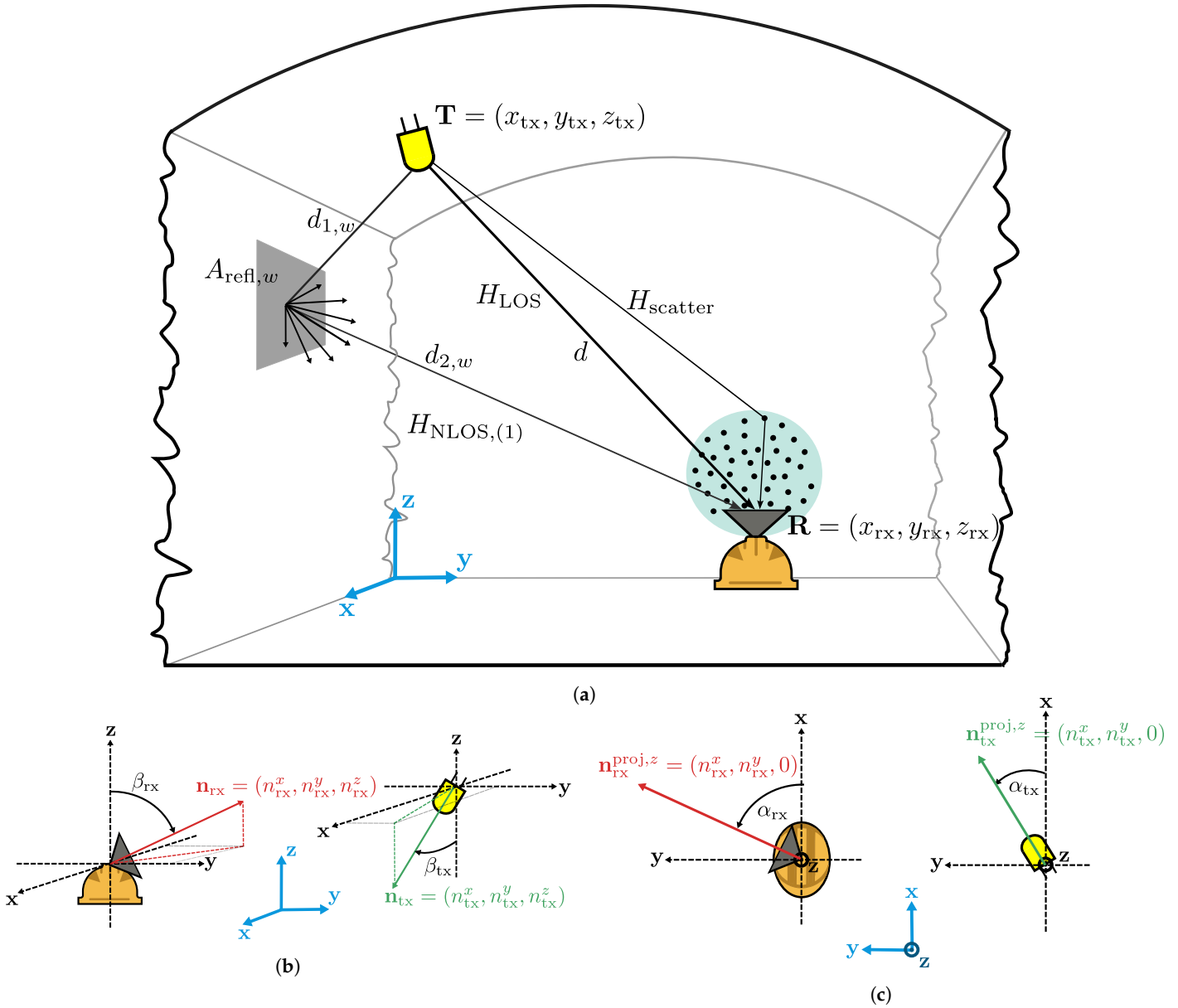


**Figure 1.** Reference UM-VLC channel model. (a) Channel components from Equation (27). (b) Tilt angles  $\beta_{rx}$  and  $\beta_{tx}$ . (c) Rotation angles  $\alpha_{rx}$  and  $\alpha_{tx}$ .

We denote  $\mathbf{n}_{tx}^{proj,z} = [n_{tx}^x, n_{tx}^y, 0]^T$  as the projection of  $\mathbf{n}_{tx}$  onto the x–y plane and  $\mathbf{n}_{rx}^{proj,z} = [n_{rx}^x, n_{rx}^y, 0]^T$  as the projection of  $\mathbf{n}_{rx}$  onto the x–y plane. Using the same definitions as [7], the RX rotation angle,  $\alpha_{rx}$ , is defined as the angle from the x-axis vector,  $[1, 0, 0]^T$  to  $\mathbf{n}_{rx}^{proj,z}$ , whereas the TX rotation angle,  $\alpha_{tx}$ , is defined as the angle from the x-axis vector,  $[1, 0, 0]^T$  to  $\mathbf{n}_{tx}^{proj,z}$ . The definitions of both rotation angles are illustrated in Figure 1c. A priori, there are no restrictions on the rotation angle values, i.e.,  $\alpha_{tx}, \alpha_{rx} \in [0, 2\pi)$ .

With these definitions, we can express  $\mathbf{n}_{tx}$  and  $\mathbf{n}_{rx}$  by [7]

$$\mathbf{n}_{tx} = \begin{bmatrix} \sin(\beta_{tx}) \cos(\alpha_{tx}) \\ \sin(\beta_{tx}) \sin(\alpha_{tx}) \\ -\cos(\beta_{tx}) \end{bmatrix} \quad \text{and} \quad \mathbf{n}_{rx} = \begin{bmatrix} \sin(\beta_{rx}) \cos(\alpha_{rx}) \\ \sin(\beta_{rx}) \sin(\alpha_{rx}) \\ \cos(\beta_{rx}) \end{bmatrix}. \tag{30}$$

### 2.3.2. Reference LOS Link

The LOS component  $H_{LOS}$  can be further expressed as [7]

$$H_{LOS} = \mathcal{C} \mathcal{G} \frac{(m+1)A_R}{2\pi d^2} \Omega_{LOS} \Psi_{LOS}, \tag{31}$$

where  $m$  is the Lambertian mode number,  $A_R$  is the PD surface area,  $d$  is the distance between LED and PD,  $\mathcal{G} \in [0, 1]$  is the optical filter gain,  $\mathcal{C} \in [1, +\infty)$  is the optical concentrator gain.  $\Omega_{LOS} \in [0, 1]$  is a trigonometric expression that depends on the relative position, rotation, and tilt of the LED and PD and the Lambertian mode number  $m$ . Finally,  $\Psi_{LOS} \in [0, 1]$  is a scaling factor that accounts for the degree of shadowing in the LOS link. Note that the dependence of  $\mathcal{C}$  and  $\mathcal{G}$  on the incident angle at the PD is implicit. We denote by  $\theta_0$  the incident angle at the PD, i.e., the angle between the incident light beam and the PD normal vector,  $\mathbf{n}_{rx}$ , which can be calculated by [7]

$$\theta_0 = \arccos\left(\frac{1}{d}(\mathbf{T} - \mathbf{R})^T \mathbf{n}_{rx}\right). \tag{32}$$

Therefore,  $\mathcal{C}$  can be expressed as

$$\mathcal{C} = \begin{cases} \frac{\eta}{\sin^2(\Theta_{FoV})} & 0 \leq \theta_0 \leq \Theta_{FoV} \\ 0 & \theta_0 > \Theta_{FoV}, \end{cases} \tag{33}$$

where  $\eta$  is the refractive index of the optical concentrator. Furthermore, the trigonometric parameter  $\Omega_{LOS}$  can be expressed as

$$\Omega_{LOS} = \left(\frac{1}{d}(\mathbf{T} - \mathbf{R})^T \mathbf{n}_{rx}\right) \times \left(\frac{1}{d}(\mathbf{R} - \mathbf{T})^T \mathbf{n}_{tx}\right)^m. \tag{34}$$

### 2.3.3. Reference NLOS Link

The single-hop NLOS component  $H_{NLOS,(1)}$  can be further expressed as [7]

$$H_{NLOS,(1)} = \frac{(m+1)A_R}{2\pi} \sum_{w=1}^W \mathcal{C}_w \mathcal{G}_w \frac{A_{\text{refl},w} \rho_w}{d_{1,w}^2 d_{2,w}^2} \Omega_{NLOS}^{(w)} \Psi_{NLOS}^{(w)}, \tag{35}$$

where  $W$  is the number of diffuse reflectors, modeled as generalized Lambertian virtual light sources (VLS) with Lambertian mode numbers equal to unity [7], such that for the  $w$ th reflector,  $A_{\text{refl},w}$  is its surface area,  $\rho_w \in [0, 1]$  is its reflectance,  $d_{1,w}$  is the distance from the LED to the reflector, and  $d_{2,w}$  is the distance from the reflector to the PD.  $\mathcal{G}_w$  and  $\mathcal{C}_w$  are the optical filter and concentrator gain at the receiver, respectively, accounting for the incident angle from the  $w$ th reflector to the PD.  $\Omega_{NLOS}^{(w)} \in [0, 1]$  is a trigonometric expression that depends on the relative position, rotation, and tilt of the LED, the  $w$ th reflector, and the PD.  $\Psi_{NLOS}^{(w)} \in [0, 1]$  is a scaling factor that accounts for the degree of shadowing in the  $w$ th NLOS link.

Consider that the  $w$ th reflector is modeled as a VLS with position  $\mathbf{R}_w = [x_w, y_w, z_w]^T$ . With this, the distance between TX and the  $w$ th reflector,  $d_{1,w}$ , is given by

$$d_{1,w} = \|\mathbf{R}_w - \mathbf{T}\|, \tag{36}$$

whereas the distance between RX and the  $w$ th reflector,  $d_{2,w}$ , is given by

$$d_{2,w} = \|\mathbf{R}_w - \mathbf{R}\|. \tag{37}$$

Additionally, the  $w$ th reflector is tilted by the tilt angle  $\beta_w \in [0, \pi]$  and rotated by the rotation angle  $\alpha_w \in [0, \pi]$ , defined in the same way as the tilt and rotation angles of the RX. The normal vector to the surface of the  $w$ -reflector is denoted by  $\mathbf{n}_w = [n_w^x, n_w^y, n_w^z]^T$  and can be calculated with [7]

$$\mathbf{n}_w = \begin{bmatrix} \sin(\beta_w) \cos(\alpha_w) \\ \sin(\beta_w) \sin(\alpha_w) \\ \cos(\beta_w) \end{bmatrix}. \tag{38}$$

Figure 2 illustrates the tilt and rotation angle definitions. We denote by  $\theta_w$  the incident angle at which the light coming from the  $w$ th reflector reaches the PD, and we calculate it by [7]

$$\theta_w = \arccos\left(\frac{1}{d_{2,w}}(\mathbf{R}_w - \mathbf{R})^T \mathbf{n}_{\text{rx}}\right). \tag{39}$$

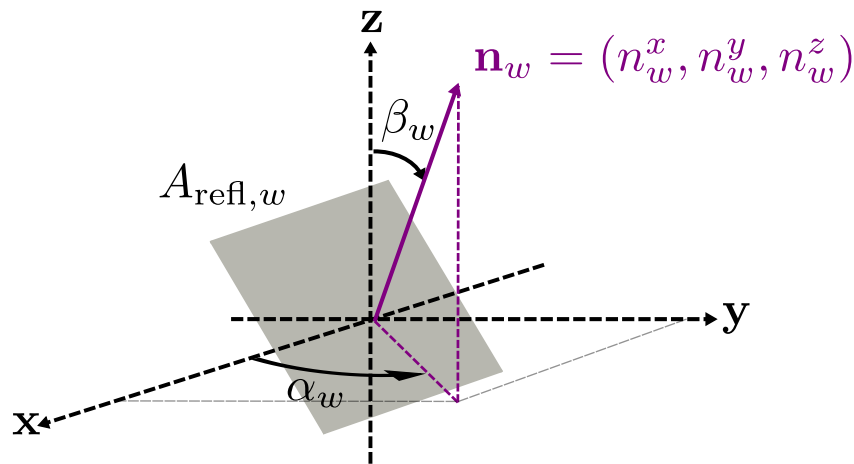


Figure 2. Tilt and rotation angles for the  $w$ th reflector.

Note that the dependence of  $C_w$  and  $G_w$  on the incident angle  $\theta_w$  is implicit. Namely,  $C_w$  can be expressed as

$$C_w = \begin{cases} \frac{\eta}{\sin^2(\Theta_{\text{FoV}})} & 0 \leq \theta_w \leq \Theta_{\text{FoV}} \\ 0 & \theta_w > \Theta_{\text{FoV}}. \end{cases} \tag{40}$$

Finally, the trigonometric parameter  $\Omega_{\text{NLOS}}^{(w)}$  can be expressed as

$$\Omega_{\text{NLOS}}^{(w)} = \left(\frac{1}{d_{2,w}}(\mathbf{R} - \mathbf{R}_w)^T \mathbf{n}_w\right) \times \left(\frac{1}{d_{2,w}}(\mathbf{R}_w - \mathbf{R})^T \mathbf{n}_{\text{rx}}\right) \times \left(\frac{1}{d_{1,w}}(\mathbf{T} - \mathbf{R}_w)^T \mathbf{n}_w\right) \times \left(\frac{1}{d_{1,w}}(\mathbf{R}_w - \mathbf{T})^T \mathbf{n}_{\text{tx}}\right)^m. \tag{41}$$

### 2.3.4. Reference Scattering Model

The NLOS scattering component  $H_{\text{scatter}}$  is defined in [7,18] as

$$H_{\text{scatter}} = \lim_{N \rightarrow \infty} \frac{(m+1)A_R \rho_s}{2N\pi} \sum_{n=1}^N \frac{p_n}{d_n^2} \Omega_{\text{scatter}}^{(n)} \Pi(\theta_n), \tag{42}$$

where  $N$  is the number of dust particles or scatterers, which tends to infinity;  $d_n$  is the total distance the light travels in its trajectory from the LED up to the  $n$ th scatterer and

then to the PD;  $\rho_s$  is the reflectance of the dust particles; and  $p_n$  is the scattering phase function for the  $n$ th scatterer.  $\Omega_{\text{scatter}}^{(n)} \in [0, 1]$  is a trigonometric expression which depends on the  $n$ th incident angle at the PD,  $\theta_n$ , on the relative position, rotation, and tilt of the LED, the  $n$ -scatterer, and the PD and on the scattering angle of the  $n$ th scatterer,  $\phi_n$ . The function  $\Pi(\cdot)$  accounts for the validity of the  $n$ th light beam, by checking whether it falls in the PD's field of view or not. Namely,

$$\Pi(\theta_n) = \begin{cases} 1 & 0 \leq \theta_n \leq \Theta_{\text{FoV}} \\ 0 & \theta_n > \Theta_{\text{FoV}}. \end{cases} \tag{43}$$

Note that  $p_n$  depends implicitly on the scattering angle  $\phi_n$ , and can be expressed as [7,18]

$$p_n = \frac{k_s^{\text{mie}}}{k_s} p_{\text{mie}}(\phi_n) + \frac{k_s^{\text{ray}}}{k_s} p_{\text{ray}}(\phi_n), \tag{44}$$

where  $k_s^{\text{mie}}$  is the scattering coefficient of the Mie scattering dust particles,  $k_s^{\text{ray}}$  is the scattering coefficient of the Rayleigh scattering air molecules,  $k_s = k_s^{\text{mie}} + k_s^{\text{ray}}$  is the total scattering coefficient,  $p_{\text{mie}}(\cdot)$  is the Mie scattering phase function, and  $p_{\text{ray}}(\cdot)$  is the Rayleigh scattering phase function.

The position of the  $N$  scatterers is described by a probability distribution function. The reference channel used in this work uses a distribution contained in a two-dimensional disk around the receiver [7]. Other distributions have been proposed, such as in [18], where a distribution contained in a three-dimensional sphere around the receiver is put forward.

### 2.3.5. Reference Source of Reflections

In order to evaluate the reference channel, a simulation scenario is defined in [7], considering two irregular walls as the source of reflections that run the length of the tunnel. Each wall has a surface area of  $L_x \times L_z$  ( $\text{m}^2$ ) and is divided by a square grid into squares of equal area  $\Delta A$  ( $\text{m}^2$ ), implying that each wall has a total of  $L_x \times L_z / \Delta A$  squares.  $\Delta A$  is a parameter that controls the resolution (hence, the accuracy) of the reflection calculation. We consider one reflector per square element of the gridded wall, with the  $w$ th having a reflective surface area of  $A_{\text{refl},w}$  (to not be confused with resolution area  $\Delta A$ ), position  $\mathbf{R}_w$ , rotation angle  $\alpha_w$ , and tilt angle  $\beta_w$ . With this, the total number of reflectors considered,  $W$ , is

$$W = 2 \frac{L_x L_z}{\Delta A}. \tag{45}$$

A common simplification is to consider the reflective area of all reflectors to be equal to a unique surface area  $A_{\text{refl}}$  [7], i.e.,

$$A_{\text{refl},w} = A_{\text{refl}}, \quad \forall w = 1, \dots, W. \tag{46}$$

In order to characterize the position  $\mathbf{R}_w$ , we can first define the set of values  $x_w, y_w$ , and  $z_w$  it can take. Note that  $x_w$  can take  $\ell_x = L_x / \Delta A$  values,  $y_w$  can take two values (one for each wall), and  $z_w$  can take  $\ell_z = L_z / \Delta A$  values, where we select  $\Delta A$  such that  $\ell_x$  and  $\ell_z$  are natural numbers. The set of possible values of  $x_w$ ,  $\mathcal{X}_W$ , is then given by

$$\mathcal{X}_W = \{x = \Delta A \times n \mid n = 0, 1, \dots, \ell_x\}, \tag{47}$$

the set of possible values of  $y_w$ ,  $\mathcal{Y}_W$ , is simply

$$\mathcal{Y}_W = \{0, L_y\} \tag{48}$$

since each wall is located at each extreme of the  $y$ -axis in the simulation scenario. The set of possible values of  $z_w$ ,  $\mathcal{Z}_W$ , is given by

$$\mathcal{Z}_W = \{z = \Delta A \times n \mid n = 0, 1, \dots, \ell_z\}. \tag{49}$$

With these definitions, the set of  $W$  possible reflector positions is given by

$$\{\mathbf{R}_1, \mathbf{R}_2, \dots, \mathbf{R}_W\} = \mathcal{X}_W \times \mathcal{Y}_W \times \mathcal{Z}_W. \tag{50}$$

To simulate diffuse reflection on irregular walls, a non-deterministic approach is employed, such that the tilt and rotation angles for the  $w$ th reflector,  $\alpha_w$  and  $\beta_w$ , respectively, are modeled as random variables independently drawn from a uniform distribution. In general, we have for the tilt angles  $\beta_w$  that

$$\beta_w \sim \mathcal{U}[0, \pi], \quad \forall w = 1, \dots, W, \tag{51}$$

whereas the rotation angles  $\alpha_w$  depend on the wall on which the  $w$ th reflector is located, namely,

$$\alpha_w \sim \mathcal{U}[0, \pi], \quad \forall w \in \{w \mid y_w = 0\}, \tag{52}$$

and

$$\alpha_w \sim \mathcal{U}[\pi, 2\pi], \quad \forall w \in \{w \mid y_w = L_y\}. \tag{53}$$

Additionally, a common simplification is that all reflectors have the same reflectance  $\rho$ , i.e.,

$$\rho_w = \rho, \quad \forall w = 1, \dots, W. \tag{54}$$

### 2.3.6. Reference Shadowing Model

In an LOS link with an arbitrary TX position,  $\mathbf{A} = [x_a, y_a, z_a]$ , and an arbitrary RX position,  $\mathbf{B} = [x_b, y_b, z_b]$ , the shadowing weight  $\Psi$ , as defined in [7], is given by

$$\Psi = \exp(-\epsilon T_s \cdot \Xi(\mathbf{A}, \mathbf{B})), \tag{55}$$

where  $\epsilon$  is known as the intensity parameter of the Poisson process which models the number of shadowing objects in a given period of time,  $T_s$ , and  $\mathcal{S}(\mathbf{A}, \mathbf{B})$  is the expected value of the probability that the LOS link is blocked by a shadowing object in the time period  $T_s$ .  $\Xi(\mathbf{A}, \mathbf{B})$  can be expressed analytically as

$$\Xi(\mathbf{A}, \mathbf{B}) = \int_0^{L_y} \int_0^{L_x} \left( \int_{\mathcal{F}(x,y;\mathbf{A},\mathbf{B})} \int_{2\mathcal{D}(x,y;\mathbf{A},\mathbf{B})} g_s(u,v) du dv \right) f_s(x,y) dx dy, \tag{56}$$

where  $g_s(u, v)$  is the joint probability density function (PDF) that describes the possible widths,  $u$ , and heights,  $v$ , of the shadowing obstacles.  $f_s(u, v)$  is the joint PDF that describes the possible  $x$ -axis coordinates,  $x$ , and  $y$ -axis coordinates,  $y$ , of the obstacles' projection midpoint in the  $x$ - $y$  plane. The function  $\mathcal{D}(x, y; \mathbf{A}, \mathbf{B})$  is defined as

$$\mathcal{D}(x, y; \mathbf{A}, \mathbf{B}) = \frac{|(y_a - y_b)x - (x_a - x_b)y - x_b y_a + x_a y_b|}{\sqrt{(y_a - y_b)^2 + (x_a - x_b)^2}}, \tag{57}$$

whereas function  $\mathcal{F}(x, y; \mathbf{A}, \mathbf{B})$  is defined as

$$\mathcal{F}(x, y; \mathbf{A}, \mathbf{B}) = \frac{(y_a - y_b)^2 + (x_a - x_b)^2 + (x - x_b)^2 + (y - y_b)^2 - (x - x_a)^2 - (y - y_a)^2}{2\sqrt{(y_a - y_b)^2 + (x_a - x_b)^2}} + z_b. \tag{58}$$

With these definitions,  $\Psi_{\text{LOS}}$  can be expressed as

$$\Psi_{\text{LOS}} = \exp(-\epsilon T_s \cdot \Xi(\mathbf{T}, \mathbf{R})), \tag{59}$$

and  $\Psi_{\text{NLOS}}^{(w)}$  as

$$\Psi_{\text{NLOS}}^{(w)} = \exp(-\epsilon T_s [\Xi(\mathbf{T}, \mathbf{R}_w) + \Xi(\mathbf{R}_w, \mathbf{R})]), \tag{60}$$

where the shadowing weights were calculated independently for the TX-reflector link and for the reflector-RX link and multiplied together, as in [7].

### 2.3.7. Reference Channel Impulse Response

If we define  $H_{\text{NLOS},w}$  as the single-hop NLOS link formed by light reflecting off the  $w$ th reflector such that

$$H_{\text{NLOS},(1)} = \sum_{w=1}^W H_{\text{NLOS},w}, \quad (61)$$

and  $H_{\text{scatter},n}$  as the NLOS link formed by light reflecting off the  $n$ th scatterer such that

$$H_{\text{scatter}} = \sum_{n=1}^N H_{\text{scatter},n}, \quad (62)$$

then the channel impulse response (CIR) for the reference model,  $h_{\text{ref}}(t)$ , can be expressed as [7]

$$h_{\text{ref}}(t) = R \left[ H_{\text{LOS}} \cdot \delta \left( t - \frac{d}{c} \right) + \sum_{w=1}^W H_{\text{NLOS},w} \cdot \delta \left( t - \frac{d_{1,w} + d_{2,w}}{c} \right) + \sum_{n=1}^N H_{\text{scatter},n} \cdot \delta \left( t - \frac{d_n}{c} \right) \right], \quad (63)$$

where  $\delta(\cdot)$  denotes the Dirac delta function. It is shown in [7,18] that the scattering component  $H_{\text{scatter}}$  is about three orders of magnitude smaller than the single-hop NLOS component and about four orders of magnitude smaller than the LOS component. Consequently,  $H_{\text{scatter}} \approx 0$  is a good approximation. In the present work, the CIR of the reference model is considered to be

$$h_{\text{ref}}(t) = R \left[ H_{\text{LOS}} \cdot \delta \left( t - \frac{d}{c} \right) + \sum_{w=1}^W H_{\text{NLOS},w} \cdot \delta \left( t - \frac{d_{1,w} + d_{2,w}}{c} \right) \right]. \quad (64)$$

### 2.4. Proposed UM-VLC Channel Model

The proposed channel model, not unlike the reference channel model, is a UM-VLC channel model that considers the relative rotation and tilt of the LED and the PD, irregular walls, shadowing, and scattering. The difference is that  $H_{\text{ref}}$  describes the channel transmission for an SISO link considering a monochromatic LED as the TX, whereas our proposed channel model takes into account a multichromatic LED and the spectral distribution of different channel parameters. Additionally, our model takes into account attenuation from light scattering and absorption caused by dust particles, which are absent from the reference model.

The DC gain of the proposed channel model for optical inputs and optical outputs takes the form

$$H_{\text{opt}} = H_{\text{LOS}}^{\text{opt}} + H_{\text{NLOS},(1)}^{\text{opt}}, \quad (65)$$

where the  $H_{\text{scatter}}$  component is not taken into account due to the small impact it has on the CIR. Instead, in our proposed model, the scattering and absorption effects due to dust particles are integrated directly into the LOS and NLOS components. In general, the DC gain of the optical channel can be expressed as [25]

$$H_{\text{opt}} = \frac{P_R}{P_T}, \quad (66)$$

where  $P_R$  is the optical power received from the PD and  $P_T$  is the optical power emitted by the LED. For an LED with spectral power distribution (SPD),  $\Phi(\lambda)$ ,  $P_T$  can be expressed as [25]

$$P_T = \int_{380 \text{ nm}}^{825 \text{ nm}} \Phi(\lambda) d\lambda. \quad (67)$$

Equivalently,  $P_R$  can be expressed as

$$P_R = \int_{380 \text{ nm}}^{825 \text{ nm}} \mathcal{A}(\lambda)\Phi(\lambda) d\lambda, \tag{68}$$

where  $\mathcal{A}(\lambda)$  represents a spectral weighting function that accounts for the power attenuation due to environmental and geometric factors. This function can be further divided into the established LOS and single-hop NLOS components, with

$$\mathcal{A}(\lambda) = \mathcal{A}_0(\lambda) + \sum_{w=1}^W \mathcal{A}_w(\lambda), \tag{69}$$

where  $\mathcal{A}_0(\lambda)$  represents the LOS link weighting function and  $\mathcal{A}_w(\lambda)$  the NLOS link weighting function for the  $w$ th reflector. Combining Equations (66), (68), and (69) with Equation (65), one finds that

$$H_{\text{LOS}}^{\text{opt}} = \frac{1}{P_T} \int \mathcal{A}_0(\lambda)\Phi(\lambda) d\lambda, \tag{70}$$

and

$$H_{\text{NLOS,(1)}}^{\text{opt}} = \frac{1}{P_T} \sum_{w=1}^W \int \mathcal{A}_w(\lambda)\Phi(\lambda) d\lambda, \tag{71}$$

where the integral limits are omitted for the sake of simplicity.

Considering Equation (68) as the definition of the optical power received, the electrical photocurrent  $I_{ph}$  produced at the PD with spectral responsivity  $R(\lambda)$  can be expressed as

$$I_{ph} = \int_{380 \text{ nm}}^{825 \text{ nm}} R(\lambda)\mathcal{A}(\lambda)\Phi(\lambda) d\lambda. \tag{72}$$

The DC gain of the proposed channel model for optical inputs and electrical outputs takes the form

$$H_{\text{el}} = \frac{I_{ph}}{P_T} = H_{\text{LOS}}^{\text{el}} + H_{\text{NLOS,(1)}}^{\text{el}}. \tag{73}$$

Combining Equations (69), (72), and (73), one finds that

$$H_{\text{LOS}}^{\text{el}} = \frac{1}{P_T} \int R(\lambda)\mathcal{A}_0(\lambda)\Phi(\lambda) d\lambda, \tag{74}$$

and

$$H_{\text{NLOS,(1)}}^{\text{el}} = \frac{1}{P_T} \sum_{w=1}^W \int R(\lambda)\mathcal{A}_w(\lambda)\Phi(\lambda) d\lambda. \tag{75}$$

#### 2.4.1. Proposed LOS Link

Using the same geometry as the reference channel model and the parameters as in Equation (31), and adding a new spectral transmittance function  $\zeta_0(\lambda)$  that accounts for the attenuation caused by scattering and absorption due to dust particles in the LOS link,  $\mathcal{A}_0(\lambda)$  can be defined as

$$\mathcal{A}_0(\lambda) = \mathcal{C} \frac{(m+1)A_R}{2\pi d^2} \Omega_{\text{LOS}} \Psi_{\text{LOS}} \mathcal{G}(\lambda)\zeta_0(\lambda), \tag{76}$$

where the optical filter gain,  $\mathcal{G}(\lambda)$ , is the only spectral parameter apart from  $\zeta_0(\lambda)$ . The optical concentrator gain,  $\mathcal{C}$ , depends on an incident angle rather than wavelength [25]; the Lambertian mode number  $m$ , PD surface area  $A_R$ , the link distance  $d$ , and the trigonometric expression  $\Omega_{\text{LOS}}$  are all geometric parameters that do not depend on the wavelength. The shadowing weighting factor  $\Psi_{\text{LOS}}$  does not depend on wavelength, as, by definition, shadowing objects



block light throughout the visible spectrum. Combining Equation (76) into Equation (70), the proposed DC gain of the optical LOS link can be expressed as

$$H_{\text{LOS}}^{\text{opt}} = c \frac{(m+1)A_R}{2\pi d^2 P_T} \Omega_{\text{LOS}} \Psi_{\text{LOS}} \int \mathcal{G}(\lambda) \zeta_0(\lambda) \Phi(\lambda) d\lambda. \quad (77)$$

Equivalently, by combining Equation (76) with Equation (74), the proposed DC gain of the electro-optical LOS link can be expressed as

$$H_{\text{LOS}}^{\text{el}} = c \frac{(m+1)A_R}{2\pi d^2 P_T} \Omega_{\text{LOS}} \Psi_{\text{LOS}} \int R(\lambda) \mathcal{G}(\lambda) \zeta_0(\lambda) \Phi(\lambda) d\lambda. \quad (78)$$

#### 2.4.2. Proposed NLOS Link

Using the same parameters as Equation (35) and adding a new spectral transmittance function  $\zeta_w(\lambda)$  that accounts for the attenuation caused by scattering and absorption due to dust particles in the NLOS link passing through the  $w$ th reflector,  $\mathcal{A}_w(\lambda)$  can be defined as

$$\mathcal{A}_w(\lambda) = \frac{(m+1)A_R}{2\pi} c_w \frac{A_{\text{refl},w}}{d_{1,w}^2 d_{2,w}^2} \Omega_{\text{NLOS}}^{(w)} \Psi_{\text{NLOS}}^{(w)} \rho_w(\lambda) \mathcal{G}_w(\lambda) \zeta_w(\lambda), \quad (79)$$

where the optical filter gain,  $\mathcal{G}(\lambda)$ , and the spectral reflectance of the  $w$ th reflector,  $\rho_w(\lambda)$ , are spectral parameters alongside  $\zeta_w(\lambda)$ . The justification for why the rest of the parameters are not considered spectral parameters is equivalent to the case of the LOS component. Combining Equation (79) into Equation (71), the proposed DC gain of the optical single-hop NLOS link can be expressed as

$$H_{\text{NLOS,(1)}}^{\text{opt}} = \frac{(m+1)A_R}{2\pi P_T} \sum_{w=1}^W c_w \frac{A_{\text{refl},w}}{d_{1,w}^2 d_{2,w}^2} \Omega_{\text{NLOS}}^{(w)} \Psi_{\text{NLOS}}^{(w)} \int \rho_w(\lambda) \mathcal{G}_w(\lambda) \zeta_w(\lambda) \Phi(\lambda) d\lambda. \quad (80)$$

Equivalently, combining Equation (79) into Equation (75), the proposed DC gain of the electro-optical single-hop NLOS link can be expressed as

$$H_{\text{NLOS,(1)}}^{\text{el}} = \frac{(m+1)A_R}{2\pi P_T} \sum_{w=1}^W c_w \frac{A_{\text{refl},w}}{d_{1,w}^2 d_{2,w}^2} \Omega_{\text{NLOS}}^{(w)} \Psi_{\text{NLOS}}^{(w)} \int R(\lambda) \rho_w(\lambda) \mathcal{G}_w(\lambda) \zeta_w(\lambda) \Phi(\lambda) d\lambda. \quad (81)$$

#### 2.4.3. Proposed Scattering and Absorption Model

To characterize the effects of dust scattering and absorption in the LOS and NLOS links, transmittance functions  $\zeta_0(\lambda)$  and  $\zeta_w(\lambda)$  must be defined. Note that in the reference channel, the Rayleigh and Mie scattering regimes contribute exclusively to the scattering-induced NLOS component  $H_{\text{scatter}}$ , while the absorption effects are not considered in any of the channel components. In contrast, our proposed channel model considers Mie (and not Rayleigh) scattering and absorption effects in both LOS and NLOS links. The exclusion of the Rayleigh regime can be justified by looking at the ratio of the size of the spherical particles to the wavelength,  $\alpha = \pi D/\lambda$  [30], where  $D$  is the diameter of the particle. If  $\alpha \ll 1$ , then the Rayleigh scattering model is valid. When wavelength and particle size are comparable, Mie scattering theory is more accurate, and when  $\alpha \gg 1$ , then geometric scattering theory is used [30]. The particle size distribution of airborne particles in underground mines varies depending on the extractive activity, mineral composition, and geology of the mine, but a generalization can be made by looking at several studies conducted in underground coal mines in the United States [31,32], China [30,33], and the former Soviet Union [34] and underground gold mines in Alaska, Nevada, and South Africa [35], all of which show that the particle sizes of coal and silica dust particle sizes are in the order of 1  $\mu\text{m}$  to 100  $\mu\text{m}$ . Taking into account the wavelengths in the visible spectrum, this range of particle sizes implies that  $\alpha$  takes values in the order of 1 to  $10^3$ : that

means that Mie theory is the preferred regime for describing the scattering and absorption phenomena in underground mines.

The attenuation of optical channels in non-ideal environments is usually modeled by the Beer–Lambert law, e.g., underwater optical channels [14,36,37], outdoor optical channels degraded by rain and snow [38] and sandstorms [39], and UM-VLC channels attenuated by coal dust [5,30]. The transmittance function  $T(\lambda)$ , according to the Beer–Lambert law, is given by [30]:

$$T(\lambda) = \exp\left(-\int_0^L B_{\text{ext}}(\lambda, \ell) d\ell\right), \tag{82}$$

where  $L$  is the total length of the optical link,  $\ell$  parameterizes the optical link from 0 to  $L$ , and  $B_{\text{ext}}$  (1/m) is known as the extinction coefficient. This extinction coefficient takes into account the loss of optical power due to scattering and absorption by dust particles. In Mie regime,  $B_{\text{ext}}$  can be expressed as [30,40]:

$$B_{\text{ext}}(\lambda, \ell) = \frac{\pi}{4} N_p(\ell) \int_{x_{p,\text{min}}}^{x_{p,\text{max}}} x_p^2 F(x_p, \ell) Q_{\text{ext}}(x_p, \lambda, m(\lambda)) dx_p, \tag{83}$$

where  $N_p(\ell)$  is the number of particles per unit volume (1/m<sup>3</sup>) at the length  $\ell$  of the optical link,  $x_p$  is the particle diameter (μm),  $F(x_p, \ell)$  is the cumulative percentage undersize mass fraction distribution function at the length  $\ell$  of the optical link.  $x_{p,\text{min}}$  and  $x_{p,\text{max}}$  are the minimum and maximum particle diameters, respectively, and  $Q_{\text{ext}}$  is the extinction efficiency factor defined by Mie theory, which depends on the particle diameter  $x_p$ , wavelength  $\lambda$ , and complex refractive index  $m(\lambda)$ . If the optical link is contained in an environment where the particle concentration and size distribution are constant, then the dependence on the optical path can be relaxed (i.e.,  $B_{\text{ext}}(\lambda, \ell) \equiv B_{\text{ext}}(\lambda)$ ,  $N_p(\ell) \equiv N_p$ , and  $F(x_p, \ell) \equiv F(x_p)$ ), and Equation (82) can be rewritten as

$$T(\lambda) = \exp(-LB_{\text{ext}}(\lambda)). \tag{84}$$

The Rosin–Rammmler (R-R) distribution is widely used in the literature to model the particle size distribution of dust that results from the crushing of solids such as coal, rocks, and other materials and has been empirically validated numerous times [41]. The authors in [30] use the R-R distribution in their calculations of the extinction coefficient of coal dust in underground mines. The authors in [34] also argue that mine dust is best described by the R-R method. Assuming mine dust follows the R-R distribution, then  $F(x_p)$  can be expressed as [30,40]:

$$F(x_p) = 1 - \exp(-(x_p/\bar{x}_p)^{n_p}), \tag{85}$$

where  $\bar{x}_p$  and  $n_p$  are parameters found empirically.  $\bar{x}_p$  is known as the characteristic size and  $n_p$  is the spread index of the distribution.

The number of coal dust particles  $N_p$  can be derived from the mass per unit volume of the mine dust (mg/m<sup>3</sup>),  $W_p$ , which can be found empirically. Given  $W_p$ ,  $N_p$  can be expressed as [30]

$$N_p = \frac{W_p}{\rho_p C_v \int x_p^3 F(x_p) dx_p}, \tag{86}$$

where  $\rho_p$  is the density of the mine dust (mg/m<sup>3</sup>) and  $C_v$  is the irregularity coefficient of the mine dust. The integration limits over the possible particle diameters are omitted for the sake of simplicity. Note that when considering a spherical particle,  $C_v = \pi/6$ .

Considering mine dust consisting of spherical particles and constant particle concentrations and size distributions over the optical link, and combining Equations (83) and (86), the extinction coefficient  $B_{\text{ext}}(\lambda)$  can be expressed as

$$B_{\text{ext}}(\lambda) = \frac{3}{2} \frac{W_p}{\rho_p} \frac{\int x_p^2 F(x_p) Q_{\text{ext}}(x_p, \lambda, m(\lambda)) dx_p}{\int x_p^3 F(x_p) dx_p}, \tag{87}$$

and from Equation (84), it follows that the spectral transmittance of mine dust for the UM-VLC channel can be expressed as

$$T(\lambda) = \exp\left(-\frac{3}{2}L \frac{W_p \int x_p^2 F(x_p) Q_{\text{ext}}(x_p, \lambda, m(\lambda)) dx_p}{\rho_p \int x_p^3 F(x_p) dx_p}\right). \tag{88}$$

Using Equation (84) and  $L = d$  for the LOS component and  $L = d_{1,w} + d_{2,w}$  for the  $w$ th reflector NLOS component,  $\zeta_0(\lambda)$  can be expressed as

$$\zeta_0(\lambda) = \exp(-dB_{\text{ext}}(\lambda)), \tag{89}$$

and  $\zeta_w(\lambda)$  can be expressed as

$$\zeta_w(\lambda) = \exp(-(d_{1,w} + d_{2,w})B_{\text{ext}}(\lambda)). \tag{90}$$

### 2.5. Proposed CSK-Based UM-VLC Channel Model

Consider a set of red, green, and blue LEDs with the same characteristics except for different SPDs, given by  $\Phi_1(\lambda)$ ,  $\Phi_2(\lambda)$ , and  $\Phi_3(\lambda)$ , respectively, spatially grouped together in such a way that their positions in space can be approximated to be the same from a great enough distance, and three PDs, each with spectral responsivity  $R(\lambda)$  and surface area  $A_R$  and filtered by either a red, green, or blue optical filter with spectral gain  $\mathcal{G}_1(\lambda)$ ,  $\mathcal{G}_2(\lambda)$ , or  $\mathcal{G}_3(\lambda)$ , respectively, spatially grouped so that their positions in space can be approximated to be the same from a great enough distance. If the distance  $d$  between the LEDs and the PDs is large enough, assuming that a unique transmitter position and a unique receiver position is a reasonable approximation, then the electro-optical UM-VLC DC channel gain from the  $i$ th LED to the  $j$ th PD, with  $i, j = 1, 2, 3$ , is given by

$$H_{\text{el}}[i, j] = H_{\text{LOS}}^{\text{el}}[i, j] + H_{\text{NLOS}}^{\text{el}}[i, j], \tag{91}$$

where  $H_{\text{LOS}}^{\text{el}}[i, j]$  is the DC gain of the LOS link, which can be expressed as

$$\begin{aligned} H_{\text{LOS}}^{\text{el}}[i, j] &= \frac{1}{P_{T,i}} \int R(\lambda) \mathcal{A}_{0,j}(\lambda) \Phi_i(\lambda) d\lambda, \\ &= C \frac{(m+1)A_R}{2\pi d^2 P_{T,i}} \Omega_{\text{LOS}} \Psi_{\text{LOS}} \int R(\lambda) \mathcal{G}_j(\lambda) \zeta_0(\lambda) \Phi_i(\lambda) d\lambda, \end{aligned} \tag{92}$$

where  $P_{T,i} = \int \Phi_i(\lambda) d\lambda$ . Similarly,  $H_{\text{NLOS}}^{\text{el}}[i, j]$  is the DC gain of the single-hop NLOS link, which can be expressed as

$$\begin{aligned} H_{\text{NLOS}}^{\text{el}}[i, j] &= \sum_{w=1}^W H_{\text{NLOS},w}^{\text{el}}[i, j], \\ &= \frac{1}{P_{T,i}} \sum_{w=1}^W \int R(\lambda) \mathcal{A}_{w,j}(\lambda) \Phi_i(\lambda) d\lambda, \\ &= \frac{(m+1)A_R}{2\pi P_{T,i}} \\ &\quad \times \sum_{w=1}^W C_w \frac{A_{\text{refl},w}}{d_{1,w}^2 d_{2,w}^2} \Omega_{\text{NLOS},i}^{(w)} \Psi_{\text{NLOS}}^{(w)} \int R(\lambda) \rho_w(\lambda) \mathcal{G}_{w,j}(\lambda) \zeta_w(\lambda) \Phi_i(\lambda) d\lambda. \end{aligned} \tag{93}$$

Note that if we consider that optical filters do not depend on incident angle  $\theta_w$ , then we can relax the definition to  $\mathcal{G}_{w,j}(\lambda) \equiv \mathcal{G}_j(\lambda)$ . Furthermore,  $\Omega_{\text{NLOS},i}^{(w)}$  depends on the  $i$ th LED, since we consider that the light that bounces off the  $w$ th reflector will have different angles of irradiance depending on the LED from which the light comes. This is to account for the irregularity of the underground tunnel walls, where a slight displacement of the light source can have great effects on the angle of reflection off the wall. Since the LEDs

are slightly displaced from each other, it is safe to assume that light from different LEDs will bounce off the walls independently. In practice, we model the  $w$ th reflector differently for each LED, such that it has a rotation angle  $\alpha_{1,w}$  and a tilt angle  $\beta_{1,w}$  for light coming from the red LED; a rotation angle  $\alpha_{2,w}$  and a tilt angle  $\beta_{2,w}$  for light coming from the green LED; and a rotation angle  $\alpha_{3,w}$  and a tilt angle  $\beta_{3,w}$  for light coming from the blue LED. For each  $w$ th reflector, these six angles are modeled as uniform random variables, drawn independently. We have for the tilt angles  $\beta_{1,w}, \beta_{2,w}, \beta_{3,w}$  that

$$\beta_{1,w}, \beta_{2,w}, \beta_{3,w} \sim \mathcal{U}[0, \pi], \quad \forall w = 1, \dots, W, \quad (94)$$

while the rotation angles  $\alpha_{1,w}, \alpha_{2,w}, \alpha_{3,w}$  depend on which wall the  $w$ th reflector is located, namely

$$\alpha_{1,w}, \alpha_{2,w}, \alpha_{3,w} \sim \mathcal{U}[0, \pi], \quad \forall w \in \{w \mid y_w = 0\}, \quad (95)$$

and

$$\alpha_{1,w}, \alpha_{2,w}, \alpha_{3,w} \sim \mathcal{U}[\pi, 2\pi], \quad \forall w \in \{w \mid y_w = L_y\}. \quad (96)$$

Figure 3 illustrates the channel components of the proposed CSK-based UM-VLC channel. Finally, the channel impulse response for the UM-VLC channel between the  $i$ th LED and the  $j$ th PD is given by [25]

$$h[i, j](t) = H_{\text{LOS}}^{\text{el}}[i, j] \cdot \delta\left(t - \frac{d}{c}\right) + \sum_{w=1}^W H_{\text{NLOS}, w}^{\text{el}}[i, j] \cdot \delta\left(t - \frac{d_{1,w} + d_{2,w}}{c}\right). \quad (97)$$

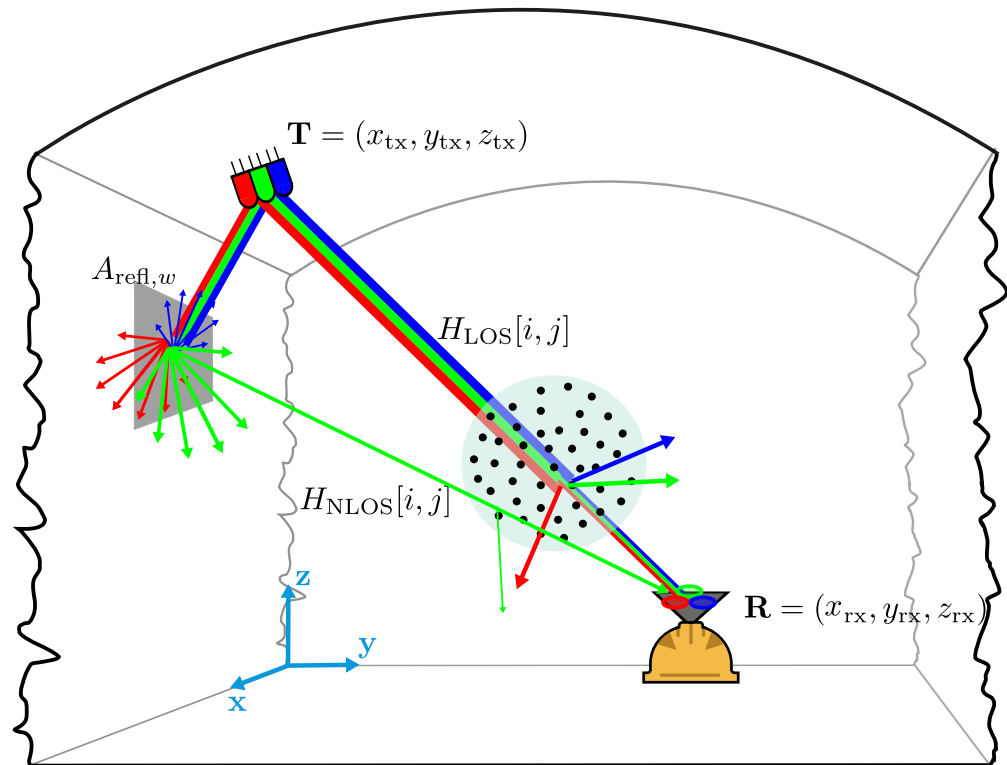


Figure 3. Proposed CSK-based UM-VLC channel model.

### 3. Results and Discussion

#### 3.1. Simulation Parameters

For the simulation scenario, we consider a mining roadway with a single CSK transmitter at a fixed position and a single CSK receiver in a miner’s helmet (hence, we position the height of RX at 1.8 m), free to move anywhere in the  $x$ – $y$  plane of the tunnel. The spatial

dimensions of the scenario and the channel parameters used in this work are defined in Table 2. All the spectral parameters used in the simulation are presented in Figure 4.

The SPDs for each LED,  $\Phi_1(\lambda)$ ,  $\Phi_2(\lambda)$ ,  $\Phi_3(\lambda)$ , are collected from [42] and were selected because they have already been used in an experimental CSK setup in [10,24]. Their dominant wavelengths are in the ranges  $\lambda_R \in [620, 645]$  (nm),  $\lambda_G \in [520, 540]$  (nm), and  $\lambda_B \in [460, 485]$  (nm) for the red, green, and blue LEDs, respectively.

**Table 2.** UM-VLC system parameters.

Parameters	Values	References
<b>Scenario</b>		
Tunnel dimensions, $L_x \times L_y \times L_z$	6 m $\times$ 3 m $\times$ 5 m	[7]
TX position, $\mathbf{T} = (x_{tx}, y_{tx}, z_{tx})$	(3, 0.5, 4.5) m	[7]
RX z-axis coordinate, $z_{rx}$	1.8 m	[7]
Spatial resolution, $(\Delta x, \Delta y, \Delta z)$	(6, 1.5, 5)/7 m <sup>2</sup>	-
Area of grid element in reflection calculation, $\Delta A$	1/9 m <sup>2</sup>	[7]
Reflective surface area of reflector element, $A_{refl}$	1 cm <sup>2</sup>	[7]
Number of reflectors per wall, $W/2$	270	[7]
with reflector rotation angles, $\alpha_{w,1}, \alpha_{w,2}, \alpha_{w,3}$	$\mathcal{U}[0, \pi]$ , wall at $y = 0$ $\mathcal{U}[\pi, 2\pi]$ , wall at $y = L_y$	[7]
with reflector tilt angle $\beta_{w,1}, \beta_{w,2}, \beta_{w,3}$	$\mathcal{U}[0, \pi]$	[7]
<b>LED parameters</b>		
Average total transmitted optical power, $P_{avg}$	10 W	[7]
Average transmitted power by $i$ th LED, $P_{avg,i}$	10/3 W	[11]
LED rotation angle, $\alpha_{tx}$	90°	-
LED tilt angle, $\beta_{tx}$	20°	-
Semi-angle at half power, $\phi_{1/2}$	60°	[7]
LED impulse response, $h_{LED}(t)$	$4(e^{-t/\tau_{fall}} - e^{-t/\tau_{rise}})$	[7,43]
LED rise time, $\tau_{rise}$	0.5 ns	[7]
LED fall time, $\tau_{fall}$	1 ns	[7]
<b>PD parameters</b>		
PD surface area, $A_R$	1 cm <sup>2</sup>	[7]
PD rotation angle, $\alpha_{rx}$	270°	-
PD tilt angle, $\beta_{rx}$	20°	-
Half angle FoV, $\Theta_{FoV}/2$	70°	[7]
Optical concentrator refractive index, $\eta$	1.5	[7]
<b>Noise parameters</b>		
Type of noise	AWGN	[25]
Electronic charge constant, $q$	$1.6 \times 10^{-19}$ C	[7]
Bandwidth of electrical filter after PD, $B$	100 MHz	[44]
Background radiation photocurrent, $I_{bg}$	10 nA	[45]
Boltzmann's constant, $\kappa$	$1.38 \times 10^{-23}$ J/K	[7]
Absolute temperature, $T_k$	295 K	[29]
Open-loop voltage gain, $G_{ol}$	10	[29]
Fixed capacitance of PD per unit area, $C_{pd}$	$112 \times 10^{-8}$ F/m <sup>2</sup>	[29]
FET channel noise factor, $\Gamma$	1.5	[29]
FET transconductance, $g_m$	0.03 S	[29]
<b>Shadowing parameters</b>		
Poisson process intensity parameter, $c$	10 per min	[46]
Poisson process time period, $T_s$	5 min	[46]
Obstacle's width and height joint PDF, $g_s(u, v)$	$\mathcal{U}(u \in [0, 1], v \in [0, 2])$	[7,46]
Obstacle's $x$ - $y$ position joint PDF, $f_s(x, y)$	$\mathcal{U}(x \in [0, 3], y \in [1, 2])$	[7,46]
<b>Dust parameters</b>		
Type of dust	Coal dust	[5]
Dust density, $\rho_p$	1450 mg/cm <sup>3</sup>	[30]
Irregularity coefficient, $C_v$	$\pi/6$	[5,30]
Mass distribution function, $F(x_p)$	$F(x_p) = 1 - \exp(-(x_p/\bar{x}_p)^{n_p})$	[30,34]
Characteristic size, $\bar{x}_p$	2 $\mu$ m	[34]
Spread index, $n_p$	0.005	[34]
Minimum particle diameter, $x_{p,min}$	1 $\mu$ m	[34]
Maximum particle diameter, $x_{p,max}$	40 $\mu$ m	[34]
Mass per unit volume of dust, $W_p$	5000 mg/m <sup>3</sup>	[34]

In datasheets such as [42], the normalized SPD  $\Phi_{\text{norm}}(\lambda)$  is usually presented in such a way that  $\max_{\lambda} \Phi_{\text{norm}}(\lambda) = 1$ . For a desired total transmitted optical power  $P$ , SPD  $\Phi(\lambda)$  can be calculated with the following expression:

$$\Phi(\lambda) = P \frac{\Phi_{\text{norm}}(\lambda)}{\int \Phi_{\text{norm}}(\lambda') d\lambda'}, \quad (98)$$

such that  $\int \Phi(\lambda) d\lambda = P$  holds.  $\Phi_{1,\text{norm}}(\lambda)$ ,  $\Phi_{2,\text{norm}}(\lambda)$ , and  $\Phi_{3,\text{norm}}(\lambda)$  used in this work are presented in Figure 4a. Note that Equation (98) implies that  $P$  does not need to be specified to calculate the channel DC components, i.e.,

$$H_{\text{opt}} = \frac{P_R}{P_T} = \frac{\int \mathcal{A}(\lambda)\Phi(\lambda) d\lambda}{\int \Phi(\lambda) d\lambda} = \frac{\int \mathcal{A}(\lambda)\Phi_{\text{norm}}(\lambda) d\lambda}{\int \Phi_{\text{norm}}(\lambda) d\lambda}, \quad (99)$$

and

$$H_{\text{el}} = \frac{I_{\text{ph}}}{P_T} = \frac{\int R(\lambda)\mathcal{A}(\lambda)\Phi(\lambda) d\lambda}{\int \Phi(\lambda) d\lambda} = \frac{\int R(\lambda)\mathcal{A}(\lambda)\Phi_{\text{norm}}(\lambda) d\lambda}{\int \Phi_{\text{norm}}(\lambda) d\lambda}. \quad (100)$$

The optical filters are the same as those used in the experimental CSK setup described in [10,24], whose spectral transmittance can be found in [47] and is presented in Figure 4b. The spectral responsivity of the PD is also the same as the one used in [10,24] and can be found in [48] and is presented in Figure 4c.

Shotcrete is a special process used for mine support as part of the new Austrian tunneling method (NATM) [49], in which concrete is sprayed onto the tunnel walls. In consequence, concrete walls are ubiquitous in modern mines. The spectral reflectance of the concrete walls was taken from [50], assuming a high-water content concrete, and is presented in Figure 4d.

The dust was assumed to be coal dust, with a refractive index taken from [30], found empirically in a coal mine in China, and presented in Figure 4e. The particle size distribution parameters of the coal dust were taken from [34], where empirical data from coal mines in the former Soviet Union were used. The work of [34] presents a wide range of possible coal dust concentrations based on different activities in the mine. A concentration of  $W_p = 5000 \text{ mg/m}^3$  was selected, which is about the highest concentration that can be obtained in coal mines without dust prevention measures according to [30] and is much higher than the maximum of  $4 \text{ mg/m}^3$  defined by the China National Health and Wellness Committee [30]. However, [34] reports dust concentrations of up to  $30 \text{ g/m}^3$  under certain mining activities. We use this high concentration value in the simulations to better exemplify the effect of dust in the communication channel.

The obstacle dimensions were selected to be uniformly distributed in the ranges of  $[0, 1] \text{ m}$  and  $[0, 2] \text{ m}$  for the width and height, respectively. Additionally, the obstacle location was selected to be uniformly distributed in ranges of  $[0, 3] \text{ m}$  and  $[1, 2] \text{ m}$  for the  $x$  and  $y$  coordinates, respectively, meaning that shadowing only occurs in one half of the tunnel in our simulation.

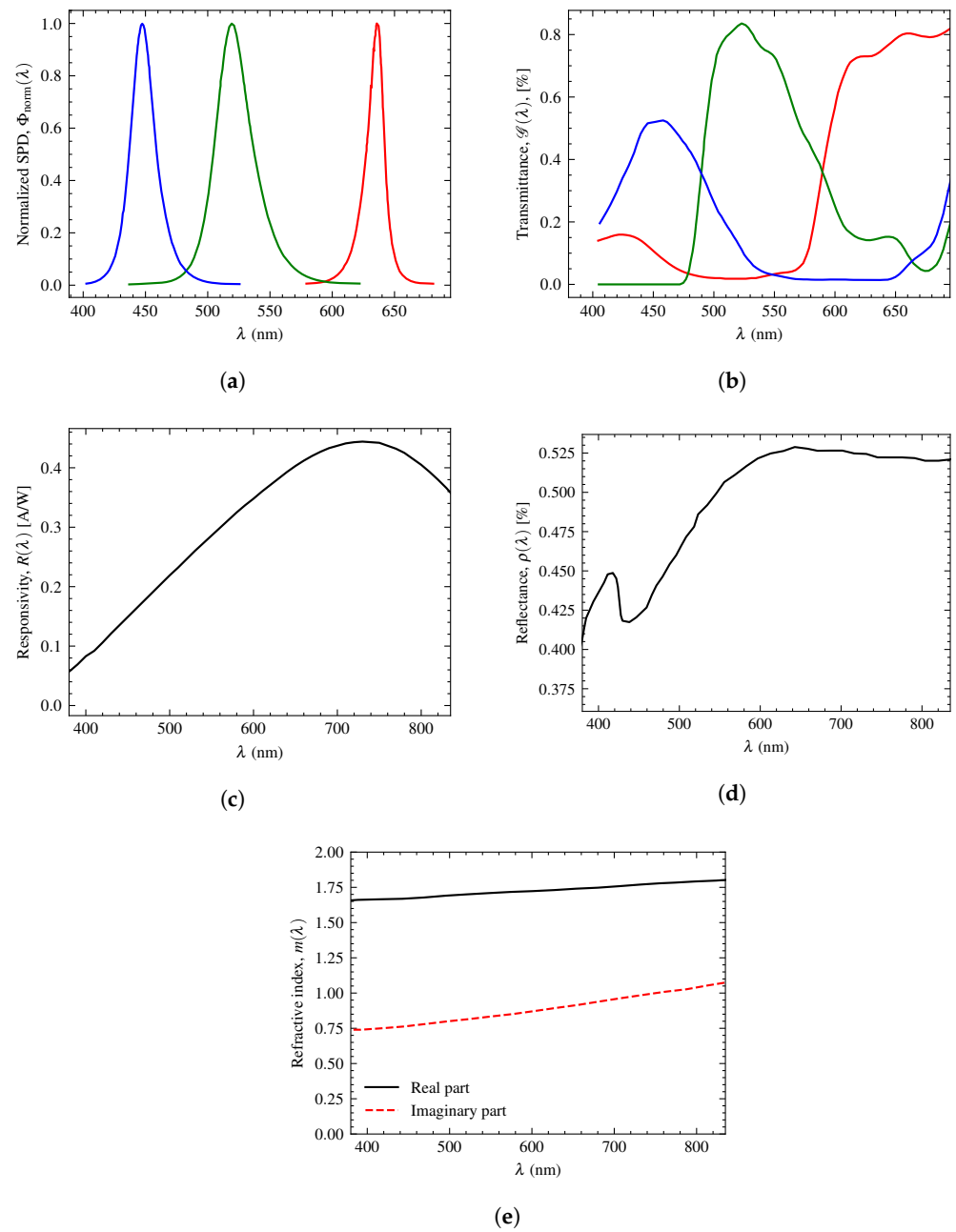


**Figure 4.** Spectral parameters used in this work: (a) Normalized SPDs of the red, green, and blue LEDs,  $\Phi_{1, \text{norm}}, \Phi_{2, \text{norm}}, \Phi_{3, \text{norm}}(\lambda)$  (colored accordingly); data from [42]. (b) Transmittance of the red, green, and blue optical filters,  $\mathcal{G}_1, \mathcal{G}_2, \mathcal{G}_3(\lambda)$  (colored accordingly); data from [47]. (c) Responsivity of the PD,  $R(\lambda)$ ; data from [48]. (d) Tunnel wall reflectance,  $\rho(\lambda)$ ; data from [50]. (e) Refractive index of dust,  $m(\lambda)$ ; data from [30].

### 3.2. Average Received Optical Power

Figure 5 shows the average results of the optical power simulation received for the proposed CSK-based UM-VLC channel model and compares it to a reference channel model consisting of a single monochromatic LED and a single PD with an optical filter gain equal to unity, i.e.,  $\mathcal{G}_{\text{ref}} = 1$ , and a wall reflectance of  $\rho_{\text{ref}} = 0.6$ . In Figure 5a, the total average optical power received (i.e., the sum of the average optical power received at the red, green, and blue PD) of the LOS link is shown over the simulation space for the proposed model, where the impact of shadowing is clearly manifested. In Figure 5b, the total average optical power received from the NLOS link is shown for the proposed model, where it is clearly observed how the two tunnel walls contribute to the received power in different ways.

The wall at  $y = 0$  is much closer to TX, and thus the closer RX is to the said wall, the more NLOS power it receives. It is also worth noting that, as should be expected, the shadowing effect is much less severe than in the LOS case. Figure 5c shows the total optical power received for the proposed model, where it can be seen how the NLOS link supplements the LOS link when the latter is shadowed, making the shadowing effect not as pronounced as in Figure 5a.

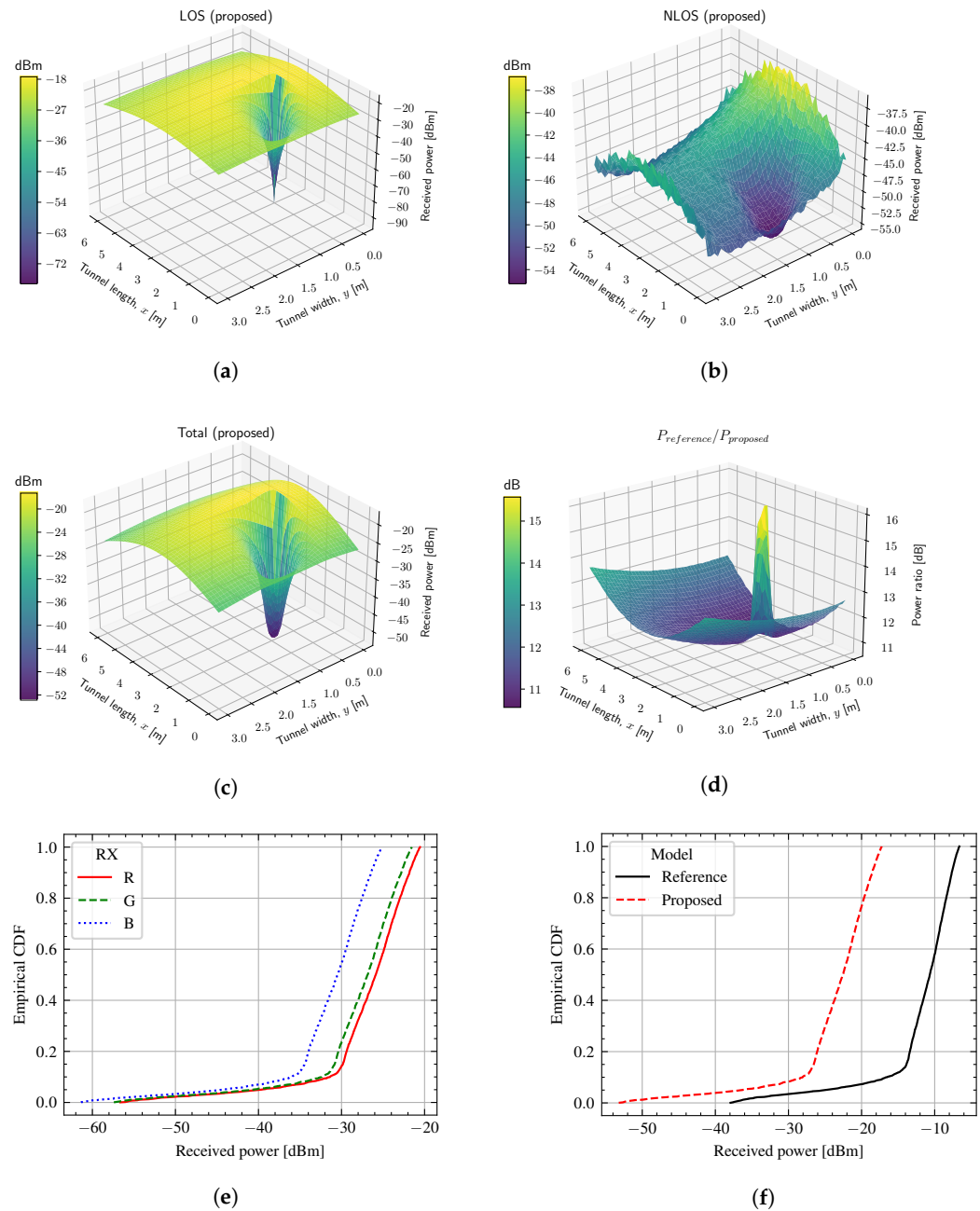


**Figure 5.** Optical power at RX. (a) Total average received power from LOS link (proposed model). (b) Total average received power from NLOS link (proposed model). (c) Total average received power (proposed model). (d) Ratio of total average received power between the reference model and the proposed model. (e) Empirical CDF for average received power at red, green, and blue PD (proposed model). (f) Empirical CDF for total average received power, comparison between the proposed model and reference model.

Figure 5d graphs the ratio between the average received optical power for the reference model and for the proposed model. It can be seen that the proposed model receives a much



lower optical power than the reference model, and this difference between the two models tends to increase the further away from the LED the RX is; this is a direct result of the dust attenuation that is factored into the proposed model, but not in the reference model. In the shadowed positions (where NLOS dominates over LOS), the difference between the two models is greater. This is explained by the fact that the NLOS link is much more affected by the dust attenuation than the LOS link, since the NLOS link tends to be longer (and thus the attenuation coefficient is larger). Figure 5e presents the empirical cumulative distribution function (ECDF) for the received optical power at the red, green, and blue PDs for the proposed model, whereas Figure 5f presents the ECDF for the total received optical power for the proposed and reference models.

### 3.3. Signal-to-Interference Ratio

Figure 6 shows the SIR simulation results for the proposed CSK-based UM-VLC channel model. In Figure 6a–c, the SIR for the red, green, and blue PD is shown over the simulation space for the proposed model. It is clear that in LOS-dominant sectors of the environment, the SIR remains fairly constant, with the blue PDs experiencing around 10 dB of interference, whereas the green and red PDs experience around 12.5 and 13.5 dB of interference, respectively. This can be easily corroborated by looking at the ECDF presented in Figure 6d, with an almost vertical cumulative distribution. The difference in interference values across the three colors can be explained by the fact that the PD spectral responsivity selected favors red and green light significantly more than blue light. The fact that the interference appears practically constant in the LOS-dominant sectors of the scenario can be explained by the fact that the refractive index of coal dust is fairly flat on the visible range, meaning that the attenuation caused by dust is not particularly color-selective, i.e., the three colors attenuate at roughly the same rate.

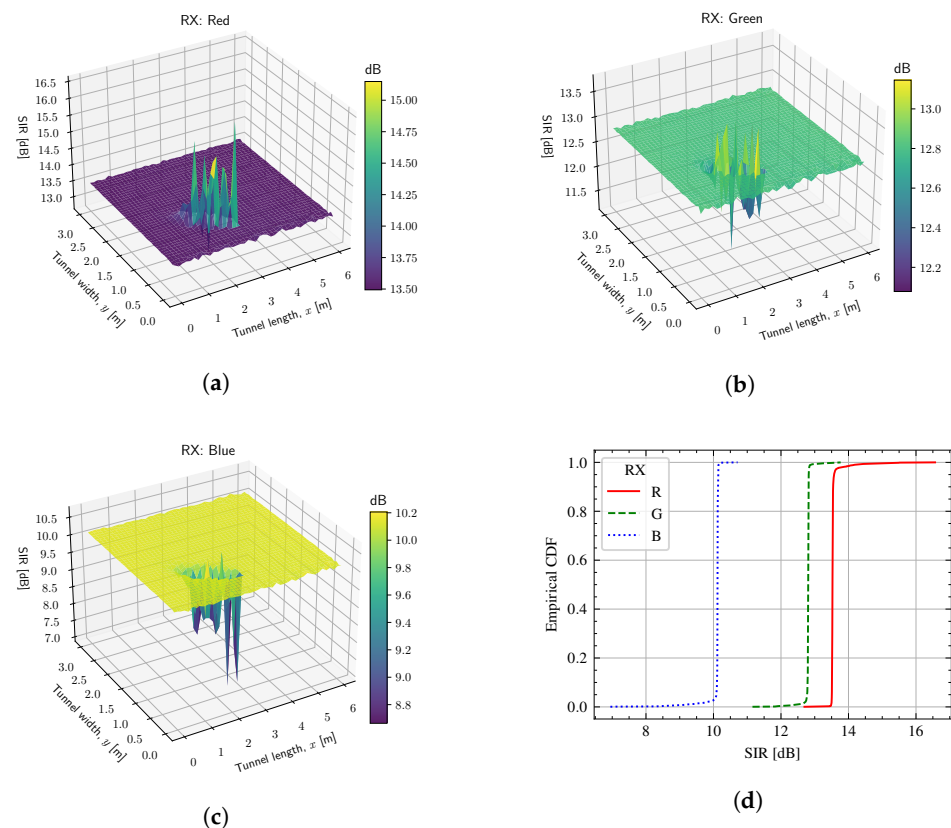


**Figure 6.** Signal-to-interference ratio. (a) Red PD. (b) Green PD. (c) Blue PD. (d) Empirical CDF for SIR at red, green, and blue PDs.

In the NLOS-dominant sectors, i.e., where the LOS link is shadowed, the SIR changes very abruptly, with the blue PD experiencing much more interference than in the LOS-dominant sectors, while the red PD experiences much less. This can be explained by the fact that the wall reflectance used in this simulation favors red and green wavelengths over blue ones.

### 3.4. Signal-to-Noise Ratio

Figure 7 shows the SNR simulation results for the proposed CSK-based UM-VLC channel model and compares it to the same reference channel model defined in Section 3.2. In Figure 7a–c, the SNR for the red, green, and blue PD is shown in the simulation space for the proposed model. Figure 7d shows the SNR for the reference model. Figure 7e presents the ECDF for the SNR of the three PDs and for the reference model. From these graphs, it is clear that the reference model can maintain a much larger SNR over the environment: most of the SNR values for the proposed model lie in the 10 to 30 dB range, whereas for the reference model, the range is 40 to 60 dB.

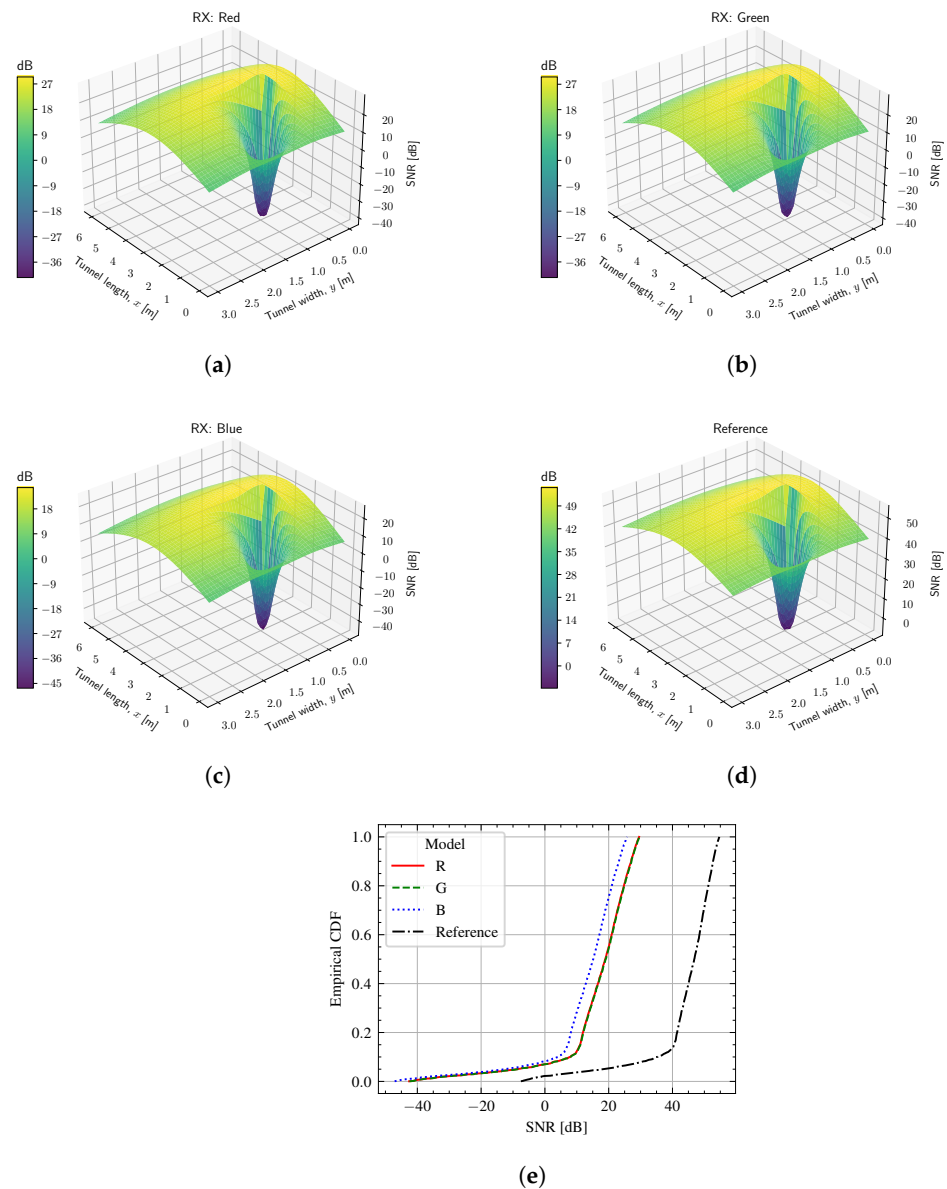


**Figure 7.** Signal-to-noise ratio. (a) Red PD. (b) Green PD. (c) Blue PD. (d) Reference model. (e) Empirical CDF for SNR at red, green, and blue PD in the proposed model, and for SNR in the reference model.

### 3.5. Channel Impulse Response

The channel impulse response is arguably the most important result when modeling a VLC channel, since it allows us to model how light signals are affected by the channel. Unfortunately, it is nearly impossible to visualize the CIR of all positions in the simulation scenario all at once. This is why Figure 8 only presents the CIR for four RX positions:  $\mathbf{R}_1 = (4, 1, 1.8)$  m,  $\mathbf{R}_2 = (2, 1, 1.8)$  m,  $\mathbf{R}_3 = (0, 3, 1.8)$  m, and  $\mathbf{R}_4 = (6, 0, 1.8)$  m. In each graph, the CIR for  $h[1, 1](t)$  (red channel),  $h[2, 2](t)$  (green channel), and  $h[3, 3](t)$  (blue channel) are compared to the CIR of the reference monochromatic channel defined in Equation (64), i.e.,  $R_{\text{ref}} \cdot h_{\text{ref}}(t)$ , where  $R_{\text{ref}} = 0.53$  A/W is the PD responsivity for the reference channel, the optical filter gain is  $\mathcal{G}_{\text{ref}} = 1$ , and the wall reflectance is  $\rho_{\text{ref}} = 0.6$ . Note that  $\mathbf{R}_1$  and  $\mathbf{R}_2$  are RX positions that are symmetrical concerning the LED, differing only in that for the RX at  $\mathbf{R}_2$ , the LOS link is severely shadowed, while for the RX at  $\mathbf{R}_1$ , there is no shadowing. Thus, comparing Figure 8a with Figure 8b allows us to clearly see the difference between an LOS-dominant and an NLOS-dominant UM-VLC channel. It is clear how, in the LOS-dominant case, i.e., Figure 8a, the reference and proposed models are similar because the RX position is close to the TX, and thus there is almost no attenuation. In the NLOS-dominant case, i.e., Figure 8b, the proposed channel is much more attenuated than the reference channel. This is as expected, since in the NLOS-dominant case, even if TX and RX are close, the light still has to travel a much longer path (to the wall and back) and thus experiences more attenuation due to dust than in the LOS-dominant case, for the same TX-RX positions. Since the dust attenuation is not factored into the reference channel, it has a much higher gain than the proposed channel in the NLOS-dominant case. The much higher delay spread present in the NLOS-dominant case is also very clear when comparing Figure 8a to Figure 8b.

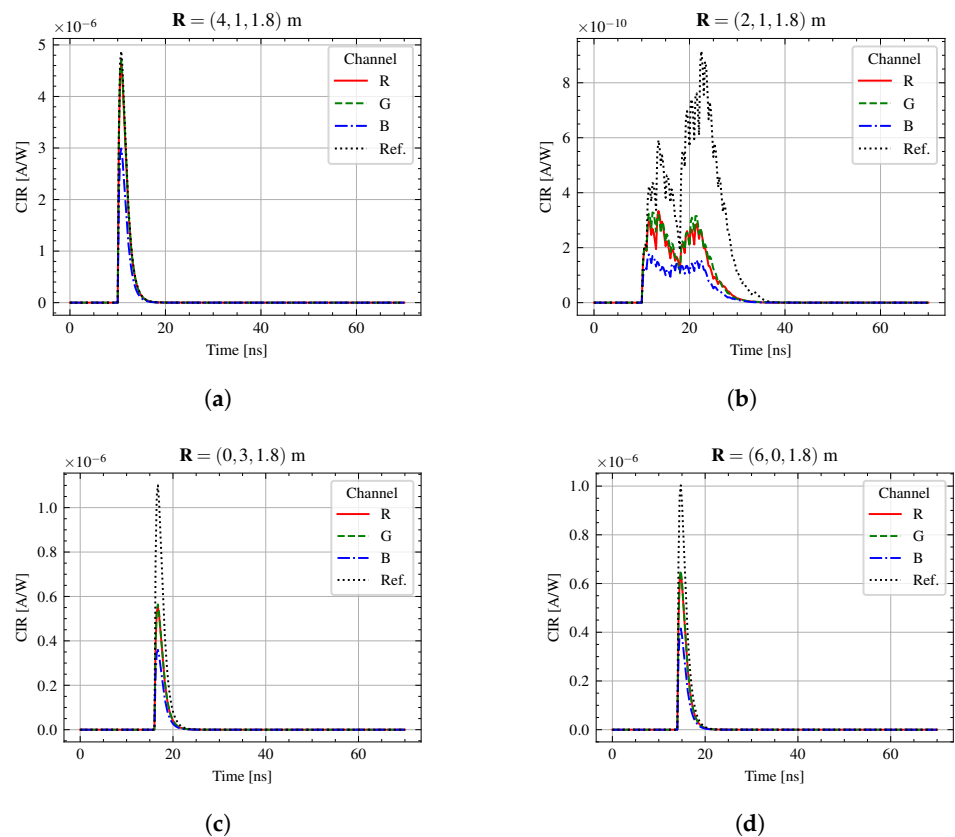


**Figure 8.** Channel impulse response. Label “R” is for  $h[1, 1](t)$ , “G” is for  $h[2, 2](t)$ , “B” is for  $h[3, 3](t)$ , and “Ref.” is for  $R_{\text{ref}} \cdot h_{\text{ref}}(t)$ . RX position at (a)  $\mathbf{R}_1 = (4, 1, 1.8)$  m, (b)  $\mathbf{R}_2 = (2, 1, 1.8)$  m, (c)  $\mathbf{R}_3 = (0, 3, 1.8)$  m, (d)  $\mathbf{R}_4 = (6, 0, 1.8)$  m.

$\mathbf{R}_3$  is located on one corner of the simulation scenario, at the wall farther away from the LED ( $y = 3$  m), whereas  $\mathbf{R}_4$  is located on another corner of the simulation scenario, at the wall closer to the LED ( $y = 0$  m). By comparing Figure 8c to Figure 8d, we see that, for the proposed channel model, the CIR of the RX located further away from the LED is slightly more attenuated than the CIR of the RX located closer to the LED. On the contrary, in the reference channel, the CIR of the RX positioned further away has a higher gain. This means that without attenuation, the corner in  $\mathbf{R}_3$  has a higher gain than the corner in  $\mathbf{R}_4$  since it is relatively better positioned to receive the radiation pattern of the LED (the LED is tilted  $20^\circ$  towards its opposite wall). This changes when considering dust attenuation, since the corner at  $\mathbf{R}_3$  is position further away than  $\mathbf{R}_4$  and thus, dust attenuation outpaces any geometrical advantage corner  $\mathbf{R}_3$  had over corner  $\mathbf{R}_4$ . In Figure 5d, we can see this even more clearly, where the power ratio is much higher in the corners at the wall farther away from the LED than in the corners at the wall closer to the LED.

### 3.6. RMS Delay

The RMS delay measures the temporal dispersion of the CIR. The RMS delay between the  $i$ th LED and the  $j$ th PD, for  $i, j = 1, 2, 3$ , can be calculated by [7]

$$\tau[i, j] = \sqrt{\frac{\int_0^\infty (t - \mu_\tau[i, j])^2 (h[i, j](t))^2 dt}{\int_0^\infty (h[i, j](t))^2 dt}}, \tag{101}$$

where  $\mu_\tau[i, j]$  is the mean delay spread and is given by

$$\mu_\tau[i, j] = \frac{\int_0^\infty t (h[i, j](t))^2 dt}{\int_0^\infty (h[i, j](t))^2 dt}. \tag{102}$$

Figure 9 shows the RMS delay results for the proposed CSK-based UM-VLC channel model and compares it with the same reference channel model defined in Section 3.2. In Figure 9a–c, the RMS delay for the red channel  $\tau[1, 1]$ , the green channel  $\tau[2, 2]$  and the blue channel  $\tau[3, 3]$  is shown over the simulation space for the proposed model. Figure 9d shows the RMS delay for the reference model, calculated using the CIR from Equation (64) with PD responsivity  $R_{ref} = 0.53$  A/W. Figure 9e presents the ECDF for the RMS of the three channels and for the reference model. It is clear that in the NLOS-dominant sectors of the simulation environment, the RMS spread is much larger. This is expected, since the NLOS link experiences more time delay as the light has to travel further. All channels, including the reference one, have almost the same RMS delay pattern. This is not surprising, since the proposed model does not modify the time components of the channel with respect to the reference model.

**Table 3.** BER simulation parameters.

Parameters	Values	References
Data rate	<b>4-CSK:</b> 24 Mb/s <b>8-CSK:</b> 72 Mb/s <b>16-CSK:</b> 96 Mb/s	[11]
IEEE 802.15.7 CSK constellation	100-010-001	[11,26]
RX samples per symbol	2 samples/symbol	-
Center-of-band wavelengths	$\lambda_1 = 632.5$ nm (red) $\lambda_2 = 530$ nm (green) $\lambda_3 = 472.5$ nm (blue)	[42]
Data bits per frame	524,232 bits	[11]
Frames transmitted per BER data point	20 frames	-
Color calibration sequence length	24 symbols	[11]

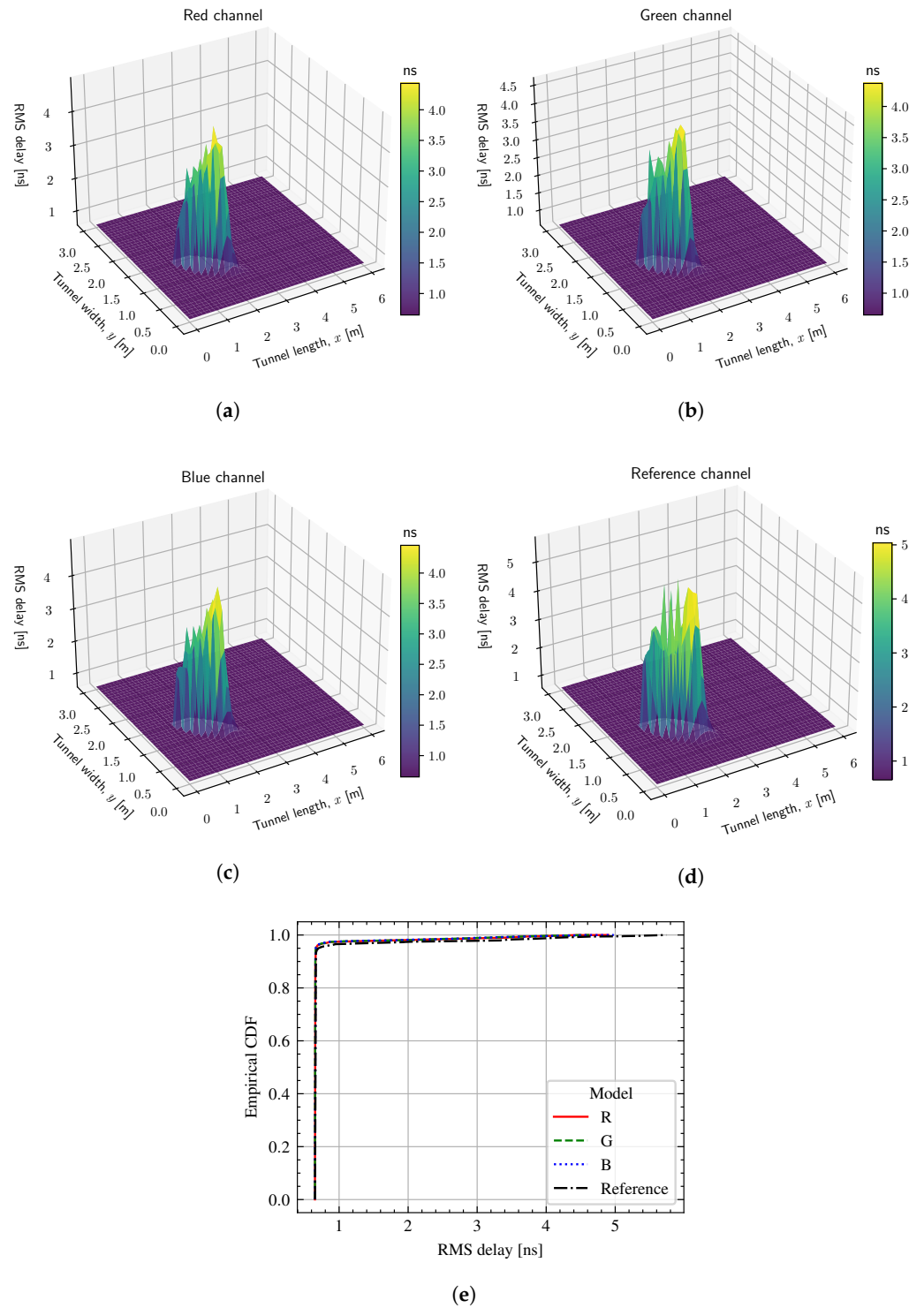


**Figure 9.** RMS delay: (a) Between red LED and red PD; (b) Between green LED and green PD; (c) Between blue LED and blue PD; (d) Reference model. (e) Empirical CDF for RMS delay for red, green, and blue channels in the proposed model and for RMS delay in the reference model.

### 3.7. Bit Error Ratio

In this section, we define a new CSK reference model whose CIR, for the channel between the  $i$ th and  $j$ th, is denoted by  $h_{\text{ref}}[i, j](t)$  and is defined as

$$h_{\text{ref}}[i, j](t) = R_{\text{ref}, j} \cdot \mathcal{G}_{\text{ref}, ij} \cdot h_{\text{LED}}(t) * h_{\text{ref}}(t), \quad (103)$$

where  $h_{\text{ref}}(t)$  is the reference channel defined in Equation (64). The reference channel defined by Equation (103) could be considered a monochromatic approximation of the CSK channel model proposed in this paper, where all the wavelength-dependency is approximated linearly, and the LEDs are considered to be monochromatic light sources of wavelengths  $\lambda_1$ ,  $\lambda_2$ , and  $\lambda_3$  for the red, green, and blue LEDs, respectively. In order to make it a fair comparison, we selected

$$\begin{bmatrix} R_{\text{ref},1} \\ R_{\text{ref},2} \\ R_{\text{ref},3} \end{bmatrix} = \begin{bmatrix} R(\lambda_1) \\ R(\lambda_2) \\ R(\lambda_3) \end{bmatrix}, \quad (104)$$

and

$$\begin{bmatrix} \mathcal{G}_{\text{ref},11} & \mathcal{G}_{\text{ref},12} & \mathcal{G}_{\text{ref},13} \\ \mathcal{G}_{\text{ref},21} & \mathcal{G}_{\text{ref},22} & \mathcal{G}_{\text{ref},23} \\ \mathcal{G}_{\text{ref},31} & \mathcal{G}_{\text{ref},32} & \mathcal{G}_{\text{ref},33} \end{bmatrix} = \begin{bmatrix} \mathcal{G}_1(\lambda_1) & \mathcal{G}_2(\lambda_1) & \mathcal{G}_3(\lambda_1) \\ \mathcal{G}_1(\lambda_2) & \mathcal{G}_2(\lambda_2) & \mathcal{G}_3(\lambda_2) \\ \mathcal{G}_1(\lambda_3) & \mathcal{G}_2(\lambda_3) & \mathcal{G}_3(\lambda_3) \end{bmatrix}, \quad (105)$$

where  $R(\lambda)$  is the spectral responsivity used in the proposed model;  $G_1(\lambda)$ ,  $G_2(\lambda)$ , and  $G_3(\lambda)$  are the transmittances of the optical filters used in the proposed model; and  $\lambda_1$ ,  $\lambda_2$ , and  $\lambda_3$  are the center-of-band wavelengths of the red, green, and blue LEDs used in the proposed model. The parameters used in the BER simulation are the same as those defined in Table 2, with the addition of parameters from Table 3. In the BER simulation,  $\sigma_j$  was not calculated with Equation (22), but rather Equation (25) was used, such that

$$\sigma_j = \sqrt{\frac{(I_{\text{avg}}[j, j])^2}{\text{SNR}}}, \quad (106)$$

where SNR is an independent variable. Given an SNR value, the BER was calculated by generating random binary sequences, modulating them with CSK and applying the proposed and reference channel models (Equations (15) and (103), respectively) to the CSK symbols, adding the noise with the corresponding standard deviation value  $\sigma_j$  (using Equation (106)), demodulating them, and applying the color calibration technique described in the IEEE 802.15.7 standard [11], in which a sequence of 24 symbols containing codes known by the receiver is sent before data transmission. A maximum of 524,232 bits of payload is to be sent per frame [11], and each frame contains one sequence for color calibration. For each SNR value, 20 frames were transmitted, meaning that about  $10^7$  bits were used to calculate each BER data point. Channel coding was not used.

The BER curves were calculated for two positions in the simulation scenario:  $\mathbf{R}_1 = (2, 1, 1.8)$  m and  $\mathbf{R}_2 = (4, 1, 1.8)$  m. These two positions were selected since they are geometrically symmetric with respect to TX, differing only in the shadowing component:  $R_1$  is heavily shadowed, while  $R_2$  is not. Figure 10 presents the resulting BER curves, Figure 10a for 4-CSK, Figure 10b for 8-CSK, and Figure 10c for 16-CSK. From these, we can clearly see that the CSK-based UM-VLC system has a considerably lower performance in the proposed channel model than in the reference channel model. There are no significant differences between the shadowed and non-shadowed RX positions, which can be explained by the fact that in this simulation, the SNR is the same for shadowed and non-shadowed RX positions, something that is not the case in simulations where the SNR is not the independent variable (e.g., see Figure 7). In the BER simulation, the main difference between the shadowed and non-shadowed RX position is the RMS delay, since it tends to be greater in NLOS-dominant positions (see Figure 9). The fact that having more RMS delay does not affect the BER performance means that this communication system is not too limited by inter-symbol interference, either because the data rate is sufficiently low or because the LED's bandwidth is sufficiently high.

The lower performance experienced by the proposed CSK-based UM-VLC channel model compared to the reference model is explained by the fact that the color distortion induced by the reference channel model can, by definition, be represented as a linear trans-

formation, which can be easily reversed by the IEEE 802.15.7 color calibration algorithm in the RX. The color distortion induced by our proposed model cannot be represented as a linear transformation but rather only approximated by one, and thus, the color calibration algorithm cannot revert its color distortion as effectively, causing the BER to increase.

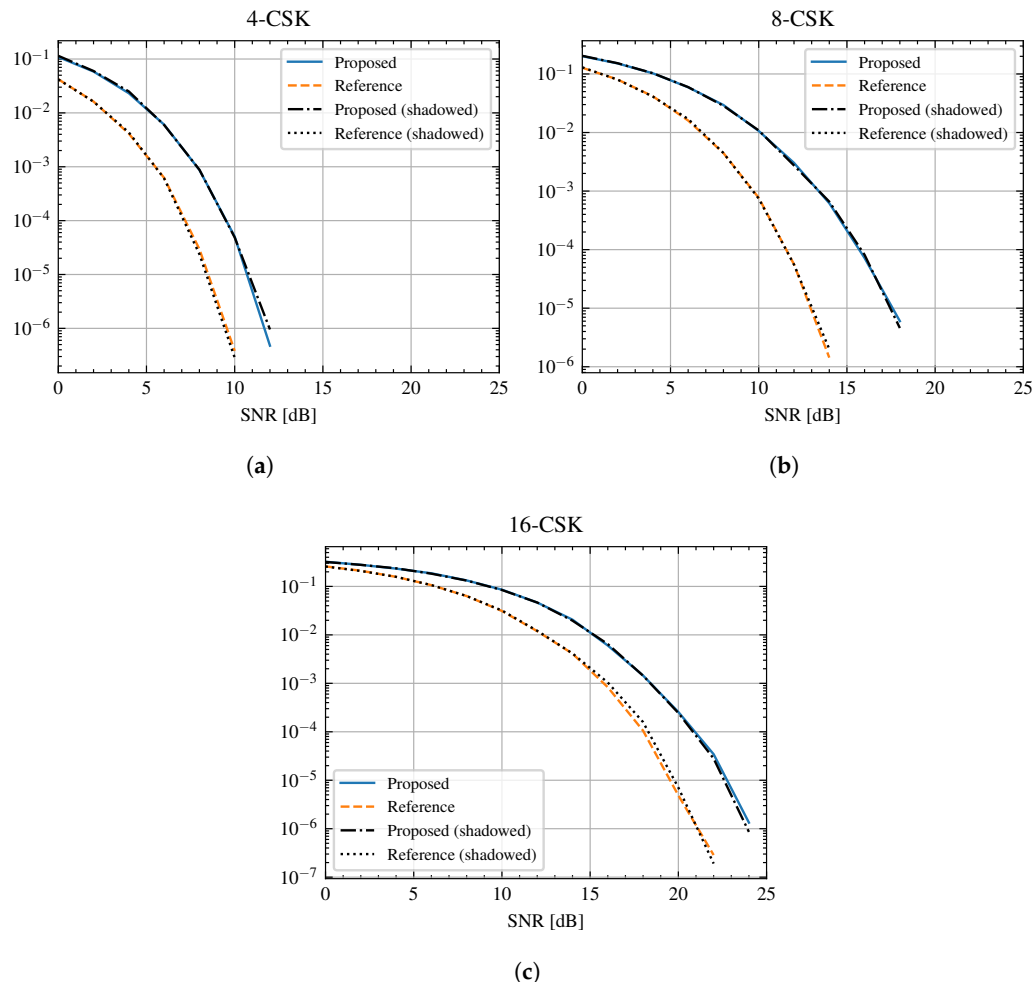


**Figure 10.** Bit error ratio curves for the proposed and reference models. Shadowed refers to RX position  $\mathbf{R}_1 = (2, 1, 1.8)$  m, while non-shadowed refers to RX position  $\mathbf{R}_2 = (4, 1, 1.8)$  m. (a) 4-CSK. (b) 8-CSK. (c) 16-CSK.

#### 4. Conclusions

We have proposed a novel wavelength-dependent SISO UM-VLC channel model. Using the ray tracing method and considering a Lambertian light source, the LOS and NLOS components of the channel were modeled taking into account the spectral characteristics of the UM-VLC channel, the relative tilt, and the rotation angle between the LP and PD, the irregular walls of the UM tunnel, shadowing by large objects, light scattering, and absorption due to dust particles.

Moreover, a novel wavelength-dependent CSK-based UM-VLC channel model was proposed on the basis of the wavelength-dependent SISO UM-VLC channel model. The CSK-based model considered three LEDs and three PDs, whose pairing forms red, green, and blue channels that interfere with each other. A simulation scenario was defined based on a mining roadway, where the TX was fixed, and the RX could move throughout the scenario. The average received optical power, the SNR, the CIR, and the RMS delay were obtained for the proposed CSK-based model and compared with a referential monochromatic state-of-the-art UM-VLC channel model in multiple LOS-dominant and NLOS-dominant RX positions of the simulated scenario. The SIR between the color

channels was also analyzed for the proposed CSK-based model, demonstrating how color interference changes between the NLOS and LOS regimes.

Finally, the BER of the proposed CSK-based UM-VLC system was obtained for two positions in the simulation scenario, and compared to a monochromatic CSK-based UM-VLC system, where color distortion was modeled as a linear transformation. It was found that the BER is significantly worse when considering the wavelength-dependent channel, as it induces non-linear color distortion that the color calibration algorithm defined by the IEEE 802.15.7 standard cannot revert effectively. With these results, we believe that we have shown that accounting for wavelength dependency has a big impact on the channel modeling of color-based VLC systems such as CSK-based VLC systems, calling for its consideration in future research.

To fully validate the proposed channel model, either on-site or test-bed experiments are to be performed in future works. On-site refers to implementing the VLC system in an actual underground mine, while test-bed refers to the implementation of an experimental setup that simulates the physical conditions of the UM-VLC channel. Furthermore, other noise models (e.g., non-Gaussian, colored, etc.) should be analyzed and experimentally verified.

**Author Contributions:** Conceptualization, R.B., C.A.A.-M., M.I. and I.S.; methodology, R.B., P.P.J., C.A.A.-M. and I.S.; software, R.B.; validation, R.B., C.A.A.-M., I.S., P.P.J., D.F.C., M.I. and J.S.; formal analysis, R.B.; investigation, R.B., C.A.A.-M. and I.S.; resources, C.A.A.-M.; data curation, R.B.; writing—original draft preparation, R.B.; writing—review and editing, R.B., P.P.J., C.A.A.-M., I.S., J.S., M.I. and D.F.C.; supervision, C.A.A.-M.; project administration, C.A.A.-M. and I.S.; funding acquisition, C.A.A.-M. and I.S. All authors have read and agreed to the published version of the manuscript.

**Funding:** This research was funded by ANID FONDECYT Regular No. 1211132 and ANID PFCHA/Beca de Doctorado Nacional/2019 21190489.

**Data Availability Statement:** The data presented in this study are available on request from the corresponding author.

**Acknowledgments:** This work was supported by Project FONDECYT Regular 1211132. This work was partially supported by CODELCO: Concurso Pienza Minería 2021; SENESCYT “Convocatoria abierta 2014-primer fase, Acta CIBAE-023-2014”; FONDEF ID21I10191; and STIC-AmSud 22-STIC-01.

**Conflicts of Interest:** The authors declare no conflict of interest.

## Abbreviations

The following abbreviations are used in this manuscript:

AWGN	Additive white Gaussian noise
BGD	Bimodal Gaussian distribution
CIE	International Commission on Illumination
CIR	Channel impulse response
CSK	Color-shift keying
DC	Direct current
ECDF	Empirical cumulative distribution function
EMI	Electromagnetic interference
FoV	Field of view
GBDM	Geometric-based deterministic model
IEEE	Institute of Electrical and Electronics Engineers
LOS	Line of sight
NATM	New Austrian tunneling method
NLOS	Non-line of sight
OOC	Optical camera communications
OOK	On-off keying
PAM	Pulse amplitude modulation
PD	Photodetector



PDF	Probability density function
R-R	Rosin–Rammler
RGB	Red, green, blue
RMS	Root mean square
RX	Receiver
SIR	Signal-to-interference ratio
SISO	Single input single output
SNR	Signal-to-noise ratio
SPD	Spectral power distribution
TX	Transmitter
UM	Underground mining
UM-VLC	Underground mining visible light communications
UWOC	Underwater wireless optical communications
UWOOC	Underwater optical camera communications
VLC	Visible light communications
VLS	Virtual light source

## References

1. Tato Diogo, M. European legal framework related to underground mining and tunnelling concerning commission directive (EU) 2017/164, 31 January establishing a fourth list of indicative occupational exposure limit values. *Int. J. Min. Sci. Technol.* **2020**, *30*, 541–545. [\[CrossRef\]](#)
2. Ranjan, A.; Zhao, Y.; Sahu, H.B.; Misra, P. Opportunities and Challenges in Health Sensing for Extreme Industrial Environment: Perspectives From Underground Mines. *IEEE Access* **2019**, *7*, 139181–139195. [\[CrossRef\]](#)
3. Yarkan, S.; Guzelgoz, S.; Arslan, H.; Murphy, R.R. Underground Mine Communications: A Survey. *IEEE Commun. Surv. Tutor.* **2009**, *11*, 125–142. [\[CrossRef\]](#)
4. Ranjan, A.; Sahu, H.B.; Misra, P. Wireless sensor networks: An emerging solution for underground mines. *Int. J. Appl. Evol. Comput.* **2016**, *7*, 1–27. [\[CrossRef\]](#)
5. Javaid, F.; Wang, A.; Sana, M.U.; Husain, A.; Ashraf, I. Characteristic study of visible light communication and influence of coal dust particles in underground coal mines. *Electronics* **2021**, *10*, 883. [\[CrossRef\]](#)
6. Wang, J.; Al-Kinani, A.; Zhang, W.; Wang, C.X. A new VLC channel model for underground mining environments. In Proceedings of the 2017 13th International Wireless Communications and Mobile Computing Conference (IWCMC), Valencia, Spain, 26–30 June 2017; pp. 2134–2139. [\[CrossRef\]](#)
7. Palacios Játiva, P.; Azurdia-Meza, C.A.; Sánchez, I.; Seguel, F.; Zabala-Blanco, D.; Dehghan Firoozabadi, A.; Gutiérrez, C.A.; Soto, I. A VLC channel model for underground mining environments with scattering and shadowing. *IEEE Access* **2020**, *8*, 185445–185464. [\[CrossRef\]](#)
8. Játiva, P.P.; Azurdia-Meza, C.A.; Zabala-Blanco, D.; Gutiérrez, C.A.; Sánchez, I.; Castillo-Soria, F.R.; Seguel, F. Bit error probability of VLC systems in underground mining channels with imperfect CSI. *AEU-Int. J. Electron. Commun.* **2022**, *145*, 154101. [\[CrossRef\]](#)
9. Miramirkhani, F.; Uysal, M. Channel modelling for indoor visible light communications. *Philos. Trans. R. Soc. A* **2020**, *378*, 20190187. [\[CrossRef\]](#) [\[PubMed\]](#)
10. Monteiro, E.; Hranilovic, S. Design and Implementation of Color-Shift Keying for Visible Light Communications. *J. Light. Technol.* **2014**, *32*, 2053–2060. [\[CrossRef\]](#)
11. *IEEE Std 802.15.7-2018 (Revision of IEEE Std 802.15.7-2011)*; IEEE Standard for Local and Metropolitan Area Networks—Part 15.7: Short-Range Optical Wireless Communications. IEEE: Piscataway, NJ, USA, 2019; pp. 1–407. [\[CrossRef\]](#)
12. Dong, K.; Ke, X.; Li, H. Camera-Based Channel Modeling and Symbol Error Rate Analysis of CSK Modulation for Outdoor OCC Systems. *IEEE Access* **2022**, *10*, 50254–50264. [\[CrossRef\]](#)
13. Shigenawa, A.; Onodera, Y.; Takeshita, E.; Hisano, D.; Maruta, K.; Nakayama, Y. Predictive Equalization for Underwater Optical Camera Communication. In Proceedings of the 2022 IEEE 95th Vehicular Technology Conference: (VTC2022-Spring), Helsinki, Finland, 19–22 June 2022; pp. 1–5. [\[CrossRef\]](#)
14. Fon, R.; Igboamalu, F.; Ndjiongue, A.; Ouahada, K.; Leke, C.; Abu-Mahfouz, A. Outage Probability of an Underwater Wireless System Based on the CSK Transmission. In Proceedings of the 2022 International Symposium on Networks, Computers and Communications (ISNCC), Shenzhen, China, 19–22 July 2022; pp. 1–6. [\[CrossRef\]](#)
15. Zhai, Y.; Zhang, S. Visible light communication channel models and simulation of coal workplace energy coupling. *Math. Probl. Eng.* **2015**, *2015*, 271352. [\[CrossRef\]](#)
16. Wang, J.; Al-Kinani, A.; Zhang, W.; Wang, C.X.; Zhou, L. A general channel model for visible light communications in underground mines. *China Commun.* **2018**, *15*, 95–105. [\[CrossRef\]](#)
17. Morales Céspedes, M.; García Armada, A. Characterization of the Visible Light Communications during the Construction of Tunnels. In Proceedings of the 2019 16th International Symposium on Wireless Communication Systems (ISWCS), Oulu, Finland, 27–30 August 2019; pp. 356–360. [\[CrossRef\]](#)

18. Palacios Játiva, P.; Azurdia-Meza, C.A.; Sánchez, I.; Zabala-Blanco, D.; Dehghan Firoozabadi, A.; Soto, I.; Seguel, F. An Enhanced VLC Channel Model for Underground Mining Environments Considering a 3D Dust Particle Distribution Model. *Sensors* **2022**, *22*, 2483. [CrossRef] [PubMed]
19. Játiva, P.P.; Azurdia-Meza, C.A.; Cañizares, M.R.; Sánchez, I.; Seguel, F.; Zabala-Blanco, D.; Carrera, D.F. Performance analysis of IEEE 802.15. 7-based visible light communication systems in underground mine environments. *Photonic Netw. Commun.* **2022**, *43*, 23–33. [CrossRef]
20. Sun, Y.; Gong, C.; Xu, Z.; Zhan, Y. Link Gain and Pulse Width Broadening Evaluation of Non-Line-of-Sight Optical Wireless Scattering Communication Over Broad Spectra. *IEEE Photonics J.* **2017**, *9*, 7900212. [CrossRef]
21. Lee, K.; Park, H.; Barry, J.R. Indoor Channel Characteristics for Visible Light Communications. *IEEE Commun. Lett.* **2011**, *15*, 217–219. [CrossRef]
22. Rodríguez, S.P.; Jiménez, R.P.; Mendoza, B.R.; Hernández, F.J.L.; Alfonso, A.J.A. Simulation of impulse response for indoor visible light communications using 3D CAD models. *EURASIP J. Wirel. Commun. Netw.* **2013**, *2013*, 7. [CrossRef]
23. Liu, W.; Zou, D.; Wang, P.; Xu, Z.; Yang, L. Wavelength dependent channel characterization for underwater optical wireless communications. In Proceedings of the 2014 IEEE International Conference on Signal Processing, Communications and Computing (ICSPCC), Guilin, China, 5–8 August 2014; pp. 895–899. [CrossRef]
24. Monteiro, E. Design and Implementation of Color-Shift Keying for Visible Light Communications. Master's Thesis, McMaster University, Hamilton, ON, Canada, 2013. Available online: <http://hdl.handle.net/11375/13484> (accessed on 4 August 2022).
25. Hoehner, P.A. *Visible Light Communications: Theoretical and Practical Foundations*; Carl Hanser Verlag GmbH Co KG: Munich, Germany, 2019; ISBN 978-3446462069.
26. Yokoi, A.; Son, J. More Description about CSK Constellation. Project: IEEE P802.15 Working Group for Wireless Personal Area Networks (WPANs). 2010. Available online: <https://mentor.ieee.org/802.15/dcn/10/15-10-0724-00-0007-csk-constellation-in-all-color-band-combinations.pdf> (accessed on 17 August 2022).
27. Tang, J.; Zhang, L.; Wu, Z. Exact Bit Error Rate Analysis for Color Shift Keying Modulation. *IEEE Commun. Lett.* **2018**, *22*, 284–287. [CrossRef]
28. Lee, E.A.; Messerschmitt, D.G. *Digital Communication*; Kluwer Academic Publishers: Amsterdam, The Netherlands, 1988.
29. Komine, T.; Nakagawa, M. Fundamental analysis for visible-light communication system using LED lights. *IEEE Trans. Consum. Electron.* **2004**, *50*, 100–107. [CrossRef]
30. Yan, J.; Wang, F.; Li, Y.; Liu, H.; Gao, Y.; Li, Z. Research on the Effect of Extinction Characteristics of Coal Dust on Visibility. *ACS Omega* **2022**, *7*, 28293–28303. [CrossRef]
31. Sapko, M.J.; Cashdollar, K.L.; Green, G.M. Coal dust particle size survey of US mines. *J. Loss Prev. Process Ind.* **2007**, *20*, 616–620. [CrossRef]
32. Organiscak, J.A.; Page, S.J.; Jankowski, R.A. *Sources and Characteristics of Quartz Dust in Coal Mines*; US Department of the Interior, Bureau of Mines: Washington, DC, USA, 1990; Volume 9271.
33. Su, X.; Ding, R.; Zhuang, X. Characteristics of dust in coal mines in central north china and its research significance. *ACS Omega* **2020**, *5*, 9233–9250. [CrossRef]
34. Lisakov, S.A.; Mikhanoshina, J.L.; Pavlov, A.N.; Sybin, E.V.; Leonov, G.V. Determination of optical radiation attenuation in dispersed system «coal dust-air». In Proceedings of the 2015 16th International Conference of Young Specialists on Micro/Nanotechnologies and Electron Devices, Erlagol, Russia, 29 June–3 July 2015; pp. 353–358. [CrossRef]
35. Chubb, L.G.; Cauda, E.G. Characterizing particle size distributions of crystalline silica in gold mine dust. *Aerosol Air Qual. Res.* **2017**, *17*, 24. [CrossRef] [PubMed]
36. Ali, M.F.; Jayakody, D.N.K.; Li, Y. Recent trends in underwater visible light communication (UVLC) systems. *IEEE Access* **2022**, *10*, 22169–22225. [CrossRef]
37. Miramirkhani, F.; Uysal, M. Visible light communication channel modeling for underwater environments with blocking and shadowing. *IEEE Access* **2017**, *6*, 1082–1090. [CrossRef]
38. Buys, J.; Janssen, L. Comparison of simultaneous atmospheric attenuation measurements at visible light, mid-infra-red (3–5  $\mu\text{m}$ ) and millimetre waves (94 GHz). *IEE Proc. H Microwaves Opt. Antennas* **1981**, *128*, 131–136. [CrossRef]
39. Ebrahim, K.J.; Al-Omary, A. Sandstorm effect on visible light communication. In Proceedings of the 2017 9th IEEE-GCC Conference and Exhibition (GCCCE), Manama, Bahrain, 8–11 May 2017; pp. 1–7. [CrossRef]
40. Marioth, E.; Koenig, B.; Krause, H.; Loebbecke, S. Fast particle size and droplet size measurements in supercritical CO<sub>2</sub>. *Ind. Eng. Chem. Res.* **2000**, *39*, 4853–4857. [CrossRef]
41. Brown, W.K.; Wohletz, K.H. Derivation of the Weibull distribution based on physical principles and its connection to the Rosin–Rammler and lognormal distributions. *J. Appl. Phys.* **1995**, *78*, 2758–2763. [CrossRef]
42. Lumileds Holding B.V. DS68 LUXEON Rebel Color Line Product Datasheet 20171106: Part No. Red: LXM2-PD01-0050, Green: LXML-PM01-0100, Blue: LXML-PB01-0040, 2017. Available online: <https://www.luxeonstar.com/assets/downloads/ds68.pdf> (accessed on 21 August 2022).
43. Son, T.T.; Burton, A.; Le-Minh, H.; Hien, D.Q. Experimental study of PC-to-PC over a visible light channel using Li-Fi USB dongle. In Proceedings of the 2019 26th International Conference on Telecommunications (ICT), Hanoi, Vietnam, 8–10 April 2019; pp. 215–219. [CrossRef]

44. Palacios Játiva, P.; Román Cañizares, M.; Azurdia-Meza, C.A.; Zabala-Blanco, D.; Dehghan Firoozabadi, A.; Seguel, F.; Montejó-Sánchez, S.; Soto, I. Interference mitigation for visible light communications in underground mines using angle diversity receivers. *Sensors* **2020**, *20*, 367. [[CrossRef](#)]
45. Chen, Y.; Sung, C.W.; Ho, S.W.; Wong, W.S. BER analysis for interfering visible light communication systems. In Proceedings of the 2016 10th International Symposium on Communication Systems, Networks and Digital Signal Processing (CSNDSP), Prague, Czech Republic, 20–22 July 2016; pp. 1–6. [[CrossRef](#)]
46. Dong, Z.; Shang, T.; Gao, Y.; Li, Q. Study on VLC channel modeling under random shadowing. *IEEE Photonics J.* **2017**, *9*, 7908416. [[CrossRef](#)]
47. LEE Filters. Polyester Filters. Part No. 024 (Scarlet), 738 (Jas Green), 079 (Just Blue). Available online: <http://www.leefilters.com/lighting/colour-details.html> (accessed on 21 August 2022).
48. Thorlabs, Inc. PDA10A2 Si Amplified Fixed Gain Detector User Guide. 2019. Available online: [www.thorlabs.us/\\_sd.cfm?fileName=TTN134700-D02.pdf&partNumber=PDA10A2](http://www.thorlabs.us/_sd.cfm?fileName=TTN134700-D02.pdf&partNumber=PDA10A2) (accessed on 21 August 2022).
49. Chen, L.; Li, P.; Liu, G.; Cheng, W.; Liu, Z. Development of cement dust suppression technology during shotcrete in mine of China-A review. *J. Loss Prev. Process Ind.* **2018**, *55*, 232–242. [[CrossRef](#)]
50. Maruthi Sridhar, B.; Chapin, T.; Vincent, R.; Axe, M.; Frizado, J. Identifying the effects of different construction practices on the spectral characteristics of concrete. *Cem. Concr. Res.* **2008**, *38*, 538–542. [[CrossRef](#)]

**Disclaimer/Publisher’s Note:** The statements, opinions and data contained in all publications are solely those of the individual author(s) and contributor(s) and not of MDPI and/or the editor(s). MDPI and/or the editor(s) disclaim responsibility for any injury to people or property resulting from any ideas, methods, instructions or products referred to in the content.